

# A new-to-nature photosynthesis system enhances utilization of one-carbon substrates in *Escherichia coli*

Received: 1 July 2024

Accepted: 13 December 2024

Published online: 02 January 2025

 Check for updatesTian Tong<sup>1</sup>, Xiulai Chen<sup>2</sup>, Kexin Tang<sup>2</sup>, Wanrong Ma<sup>2</sup>, Cong Gao<sup>2</sup>, Wei Song<sup>3</sup>, Jing Wu<sup>3</sup>, Xiaoling Wang<sup>1</sup>, Gao-Qiang Liu<sup>1</sup>✉ & Liming Liu<sup>2</sup>✉

Photosynthesis harvests solar energy to convert CO<sub>2</sub> into chemicals, offering a potential solution to reduce atmospheric CO<sub>2</sub>. However, integrating photosynthesis into non-photosynthetic microbes to utilize one-carbon substrates is challenging. Here, a photosynthesis system is reconstructed in *E. coli*, by integrating light and dark reaction to synthesize bioproducts from one-carbon substrates. A light reaction is reconstructed using the photosystem of photosynthetic bacteria, increasing ATP and NADH contents by 337.9% and 383.7%, respectively. A dark reaction is constructed by designing CO<sub>2</sub> fixation pathway to synthesize pyruvate. By assembling the light and dark reaction, a photosynthesis system is established and further programmed by installing an energy adapter, enabling the production of acetone, malate, and α-ketoglutarate, with a negative carbon footprint of −0.84 ~ −0.23 kgCO<sub>2</sub>e/kg product. Furthermore, light-driven one-carbon trophic growth of *E. coli* is achieved with a doubling time of 19.86 h. This photosynthesis system provides a green and sustainable approach to enhance one-carbon substrates utilization in the future.

Natural photosynthesis, consisting of light and dark reactions, converts solar energy and atmospheric CO<sub>2</sub> into biomass, which can be used as food, timber, and biofuels<sup>1–4</sup>. However, the large-scale implementation of natural photosynthesis faces significant challenges due to constraints, such as competition for agricultural and forestry resources vital to human survival, difficulties in processing cellulosic biomass, and uncertainties in climatic conditions<sup>5,6</sup>. Cyanobacteria and algae have harnessed their inherent photosynthetic capabilities to establish light-driven microbial cell factories, effectively addressing some of these constraints and enabling carbon-negative biomanufacturing<sup>7–9</sup>. Despite these advancements, new challenges have emerged, including the limited availability of synthetic biology toolkits, prolonged growth cycles, and the need to enhance productivity to meet industrial demands<sup>10</sup>. To overcome these challenges,

new-to-nature photosynthesis system (NPS) has garnered significant interest by restructuring and mimicking the key structural elements and functions of natural photosynthesis, this approach is expected to revolutionize agriculture and significantly reduce the carbon footprint<sup>11–13</sup>.

NPS have been proven to efficiently capture solar energy and convert CO<sub>2</sub> into valuable chemicals<sup>14</sup> and can be generally categorized into hemi-NPS and holo-NPS. Recently, hemi-NPS have been developed from the hybridization of photoelectrochemical devices<sup>15</sup> (e.g., artificial leaf<sup>16</sup> and photochemical diodes<sup>17</sup>) with microbial cells to whole-cell photosensitization<sup>18,19</sup>. In hemi-NPS, natural metabolic pathways and multi-enzyme cascade reactions effectively convert simple feedstocks (e.g., CO<sub>2</sub>, H<sub>2</sub>, and N<sub>2</sub>) into valuable chemicals<sup>20,21</sup>. Advances in synthetic biology have expanded the range of hemi-NPS products from

<sup>1</sup>Hunan Provincial Key Laboratory for Forestry Biotechnology and International Cooperation Base of Sci-Tech Innovation on Forest Resource Biotechnology, Yuelushan Laboratory of Hunan Province, Central South University of Forestry and Technology, Changsha, China. <sup>2</sup>School of Biotechnology and Key Laboratory of Industrial Biotechnology of Ministry of Education, Jiangnan University, Wuxi, China. <sup>3</sup>School of Life Sciences and Health Engineering, Jiangnan University, Wuxi, China. ✉e-mail: [gaoliuedu@csuft.edu.cn](mailto:gaoliuedu@csuft.edu.cn); [mingll@jiangnan.edu.cn](mailto:mingll@jiangnan.edu.cn)

small-molecule chemicals (e.g., acetate<sup>22,23</sup>, isopropanol<sup>24</sup>, butyrate, and threonine<sup>25</sup>) to more complex products (e.g., carotenoids, poly  $\beta$ -hydroxybutyrate (PHB)<sup>26</sup>, and proteins<sup>21</sup>). However, despite the relatively high product selectivity of hemi-NPS, they are constrained by sluggish charge transfer kinetics at the biohybrid interface<sup>27</sup>, biotoxicity, and the non-self-regeneration of photosensitizers<sup>28</sup>. To address these limitations, holo-NPS have attracted widespread attention due to their use of biogenic, genetically tractable, and stable components. Recent progress in holo-NPS includes the integration of proteorhodopsin (PR) into *E. coli* for light-driven ATP generation<sup>29</sup>, the insertion of a rhodopsin protein from *Ustilago maydis* into the vacuole membrane of *S. cerevisiae* to enhance heterotrophic metabolism<sup>30,31</sup>, the encapsulation of plant-derived photosynthesis systems into chondrocytes to increase intracellular ATP and NADPH levels for improved anabolism<sup>32</sup>, and the introduction of cyanobacteria into *S. cerevisiae* to establish endosymbiotic holo-NPS for cell growth<sup>33</sup>. Although these holo-NPS have successfully demonstrated bioenergetic and anabolic functions within cells, further enhancing the adaptability and tunability between the conversion efficiency of solar energy to metabolic energy and the biosynthetic efficiency of host cells is essential to fully realize the potential of holo-NPS.

In this study, a new-to-nature photosynthesis system (NPS) comprising a light reaction, dark reaction, and energy adapter is developed and integrated into *E. coli* (Fig. 1). The light reaction is achieved by constructing a biogenic photosystem to generate intracellular ATP and NADH, while the dark reaction is established through a synthetic CO<sub>2</sub> fixation pathway. The energy adapter, consisting of an energy responder and a protein capacitor, is designed to dynamically match light and dark reactions. This system is further programmed and optimized to enable *E. coli* to utilize one-carbon substrates for the synthesis of acetone, malate, and  $\alpha$ -ketoglutarate with a negative

carbon footprint, as well as to support light-driven one-carbon trophic growth.

## Results

### Designing and constructing of a light reaction

To engineer *E. coli* for the conversion of light energy into ATP and NADH through a light reaction, a biogenic photosystem, NPM\*, was constructed. This system was designed by assembling a backbone proteins complex, NuoK\* + PufL, and incorporating magnesium protoporphyrin IX (MgP) molecules (Fig. 2a). The backbone proteins NuoK\* + PufL comprised of the anchor protein NuoK\* and the core protein PufL, which is part of the photosynthesis reaction center. The anchor protein NuoK\* localized the biogenic photosystems NPM\* to the inner membrane (IM), while the core protein PufL, capable of binding MgP, an analog of bacteriochlorophyll a molecule, facilitated photoelectron generation. In addition, methanol served as the electron donor for the biogenic photosystem NPM\*.

To construct a backbone protein and localize it on the IM of *E. coli*, anchor proteins were evaluated and fused with the core proteins of the photosynthesis reaction center. Firstly, three anchor proteins, NuoA, NuoJ, and NuoK, were initially identified by analyzing the transmembrane topology of the 13 subunits of the NADH dehydrogenase complex (NuoA-N)<sup>34</sup>. These anchor proteins were chosen due to their association with complex I of the electron transport chain (ETC), responsible for the transfer of electrons from NADH (Supplementary Fig. 1a). To investigate their distribution in the IM of *E. coli*, fusion proteins NuoA+EGFP, NuoJ+EGFP, and NuoK+EGFP were constructed. The NuoK+EGFP was uniformly colocalized with the membrane dye FM4-64 on the IM (Fig. 2b), and its mean pixel intensity was higher than those of the control, NuoA+EGFP, and NuoJ+EGFP, respectively (Supplementary Fig. 1b). Therefore, the NuoK was chosen

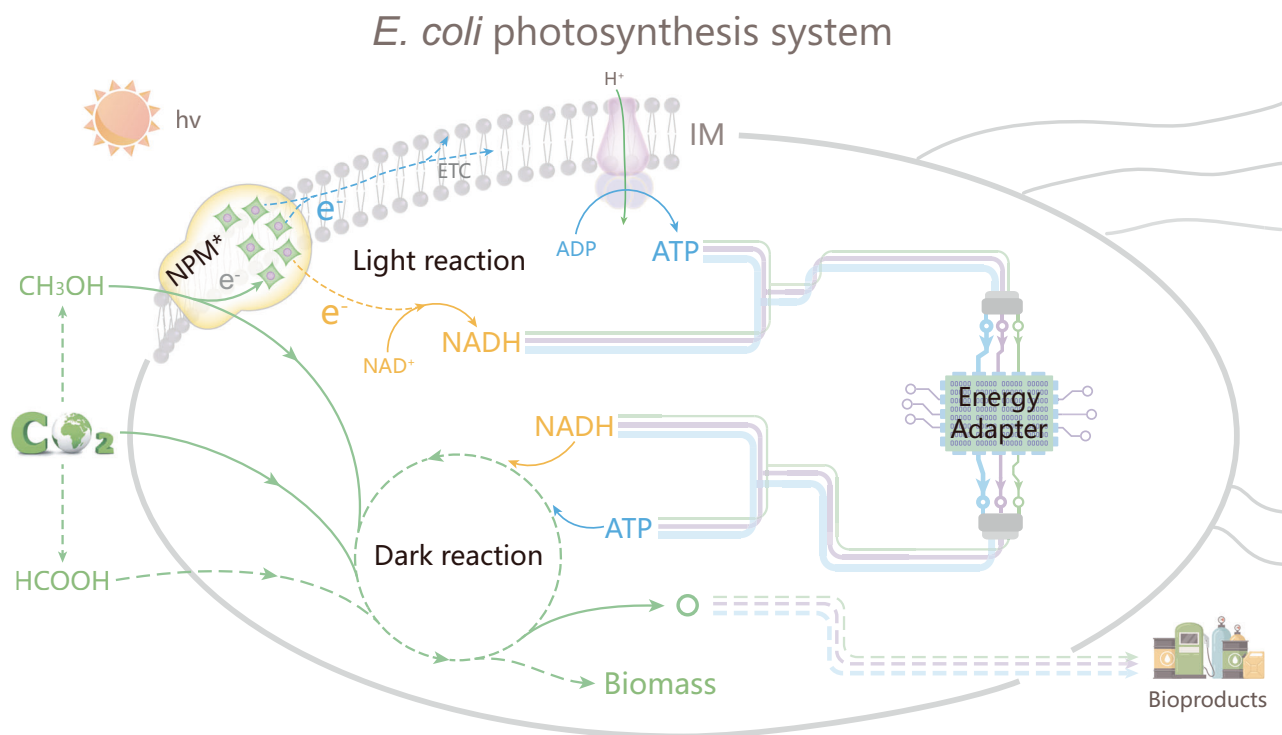
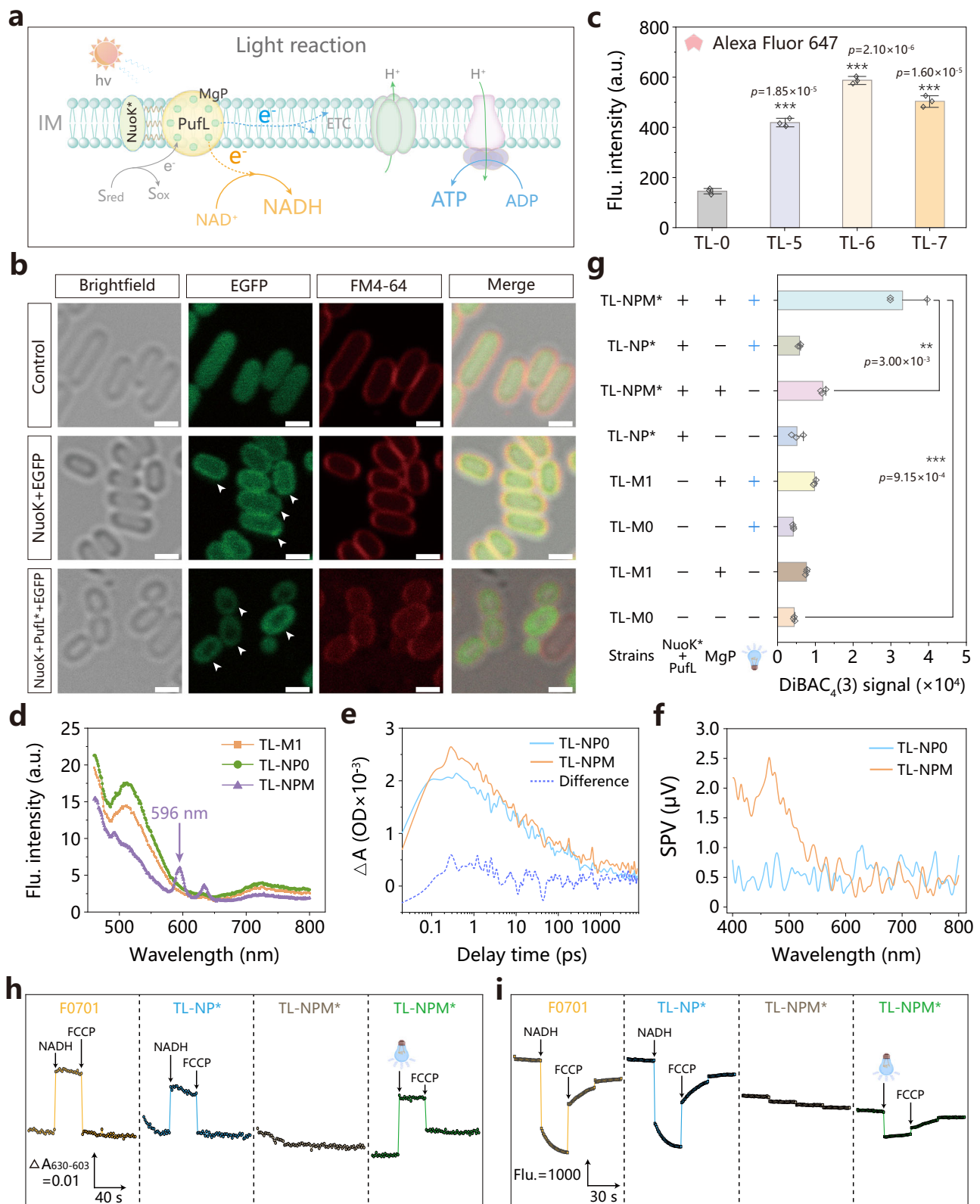


**Fig. 1 | New-to-nature photosynthesis system in *E. coli* for one-carbon substrates utilization.** *E. coli* photosynthesis system contains light reaction, dark reaction, and energy adapter. The light reaction converts light energy into metabolic energy, such as ATP and NADH by constructing a biogenic photosystem NPM\*. Dark reaction utilizes CO<sub>2</sub> to synthesize central metabolite and further expands to the output of various bioproducts driven by the light reaction. An Energy adapter is installed to dynamically match light reactions and dark reactions.

Abbreviations: hv, photon energy; e<sup>-</sup>, electron; CO<sub>2</sub>, carbon dioxide; CH<sub>3</sub>OH, methanol (as an electron sacrificial agent for NPM\*); HCOOH, formate; IM, inner membrane; ETC, electron transport chain; NPM\*, biogenic photosystem NuoK\* + PufL + MgP (NuoK\*, the mutant of NADH dehydrogenase complex subunit K; PufL, core protein of photosynthesis reaction center from *Rhodospseudomonas viridis*; MgP, magnesium protoporphyrin IX); ATP/ADP, adenosine triphosphate/diphosphate; NADH/NAD<sup>+</sup>, nicotinamide adenine dinucleotide reduced/oxidized.



as the anchor protein. Secondly, four core proteins of the photosynthesis reaction center, *crePsbA*, *PscA*, *PufL*, and *soePsbA*, were selected based on their transmembrane topology, which enables them to bind chlorophyll molecules (Supplementary Fig. 2a). Backbone proteins were then constructed by fusing *NuoK* with *crePsbA*, *PufL*, and *soePsbA* to form *NuoK+crePsbA*, *NuoK+PufL*, and *NuoK+soePsbA*, respectively. To detect the assembly of these backbone

proteins on the IM, the average fluorescence intensity of strains harboring *NuoK+crePsbA*, *NuoK+PufL*, and *NuoK+soePsbA* was assessed using immunofluorescence probes Alexa-Fluor 647 to detect His-tag localized on the periplasmic side (strains TL-5, TL-6, and TL-7, Supplementary Figs. 2b and 3), and flow cytometry to detect EGFP-tag localized on the cytoplasmic side (strains TL-8, TL-9, and TL-10, Supplementary Fig. 4). The results showed that the average fluorescence

**Fig. 2 | Designing and constructing light reaction in *E. coli*.** **a** Schematic diagram of light reaction in *E. coli*. Abbreviation: hv, photon energy; e<sup>-</sup>, electron; IM, inner membrane; ETC, electron transport chain; NuoK\*, the mutant of NADH dehydrogenase complex subunit K; PufL, core protein of photosynthesis reaction center from *Rhodospseudomonas viridis*; MgP, magnesium protoporphyrin IX; S<sub>red</sub>/S<sub>ox</sub>, redox species in reduced/oxidized form (methanol was used as an electron donor for photosystem in this study); ATP/ADP, adenosine triphosphate/diphosphate; NADH/NAD<sup>+</sup>, nicotinamide adenine dinucleotide reduced/oxidized. **b** A zoomed-in detail of fluorescence microscope images from laser confocal microscopy for strains TL-1 (control), TL-4 (NuoK + EGFP), and TL-9 (NuoK + PufL\* + EGFP). The white scale bar at the bottom right of the microscope image represented 1.0 μm. Cells pointed by white triangular arrows had significant differences in microscope images. Abbreviation: EGFP, enhanced green fluorescent protein. **c** The Alexa Fluor 647 fluorescence intensity of strains TL-0, TL-5, TL-6, and TL-7. **d** The fluorescence emission spectrum of membrane fraction suspensions for strains TL-MI, TL-NPO, and TL-NPM at 424 nm excitation wavelength. **e** The difference in transient raw

spectra for strains TL-NPO and TL-NPM at 417 nm (center of the ground state bleach region, see Supplementary Fig. 9). To extract the kinetics of MgP molecules in strain TL-NPM, the difference was obtained by subtracting the kinetics at 417 nm from strain TL-NPM and strain TL-NPO. The difference spectra represented the transient kinetics of intracellular MgP molecules. **f** The SPV curves of strains TL-NPO and TL-NPM. **g** The DiBAC<sub>4</sub>(3) fluorescence signal of strains TL-MO, TL-MI, TL-NP\*, and TL-NPM\* with or without blue light illumination. **h, i** The signal of membrane potential probe oxonol VI (**h**) and proton gradient probe ACMA (**i**) for membrane fractions of strains F0701, TL-NP\*, and TL-NPM\*. Abbreviation: ΔA<sub>630-603</sub>, absorbance change at 630 nm minus 603 nm; FCCP, carbonyl cyanide 4-(trifluoromethoxy)phenylhydrazone, an uncoupler of oxidative phosphorylation. Values were shown as mean ± s.d. from three biological replicates (**c, g**). All experiments were repeated independently three times with similar results (**b, d–f, h, i**). \**p* < 0.05, \*\**p* < 0.01, \*\*\**p* < 0.001, n.s., no significance, as determined by two-sided *t* test. Source data are provided as a Source Data file.

intensity of strains harboring NuoK+PufL (TL-6 and TL-9) was higher than that of the other strains (Fig. 2c and Supplementary Fig. 5a, b). In addition, fluorescence microscopy images of strain TL-9 showed that NuoK + PufL\* + EGFP was uniformly colocalized with FM4-64 in the IM (Fig. 2b, Supplementary Figs. 5c and 6). The fluorescence intensity of membrane fractions further indicated that NuoK + PufL\* + EGFP exhibited high assembly efficiency on the IM (Supplementary Fig. 7). These results confirmed that backbone protein NuoK + PufL was successfully constructed and assembled into the IM of *E. coli*.

To achieve photoelectric conversion of biogenic photosystems, the metalloporphyrin compound MgP was synthesized and assembled into the backbone protein NuoK + PufL in *E. coli* (Fig. 2a). Firstly, the photoelectron excitation property of MgP molecules at 450–460 nm (blue light) was demonstrated through surface photovoltaic spectroscopy and in situ ultrafast transient absorption spectroscopy (TAS) (Supplementary Figs. 8–10 and Supplementary Note 1). Methanol was identified as an electron donor for MgP molecules by evaluating the photocatalytic activity for degrading dyes Rhodamine B (RhB) and Congo red under blue light illumination (Supplementary Fig. 11 and Supplementary Note 2). MgP molecules were then successfully synthesized in vivo by introducing the heterologous MgP biosynthesis pathway<sup>35</sup>, thereby connecting to the native porphyrin metabolism (protoporphyrin IX as a precursor for MgP biosynthesis) in *E. coli* (Supplementary Figs. 12–14 and Supplementary Note 3). To assemble intracellular MgP molecules with the backbone protein NuoK + PufL (Supplementary Fig. 15 and Supplementary Note 4), the MgP biosynthetic pathway was introduced into strain TL-NP (expressing backbone protein NuoK + PufL), generating strain TL-NPM. The fluorescence emission spectrum of the membrane fraction from strain TL-NPM exhibited a significant fluorescence intensity peak at an emission wavelength of 596 nm compared with those of strains TL-MI and TL-NPO (Fig. 2d and Supplementary Fig. 16). Further analysis of the transient kinetics of intracellular MgP molecules in strain TL-NPM revealed an electron transfer time of approximately 44.07 ps (Fig. 2e and Supplementary Note 5). In addition, the surface photovoltage (SPV) of strain TL-NPM was a ~3.7-fold higher than that of strain TL-NPO at 450–460 nm (Fig. 2f). These results indicated that the biogenic photosystem (NuoK + PufL + MgP, NPM) was successfully constructed and capable of generating photoelectrons in *E. coli*.

To assess the feasibility of using the light reaction for metabolic energy generation, changes in membrane potential, proton gradient, and intracellular energy levels were examined. Firstly, NPM\* (NuoK<sup>E36A/E72Q</sup> + PufL + MgP) was confirmed as an alternative electron source for the native ETC, traditionally powered by NADH (Supplementary Fig. 17 and Supplementary Note 6). Subsequently, the changes in membrane potential of strain TL-NPM\* were evaluated using the dyes DiBAC<sub>4</sub>(3) and DiSC<sub>3</sub>(5) under blue light illumination. The results showed a 175.9% increase in fluorescence intensity with DiBAC<sub>4</sub>(3) and a 150.4% with

DiSC<sub>3</sub>(5), compared to the dark condition (Fig. 2g and Supplementary Fig. 18). In addition, the changes in membrane potential and proton gradient of membrane fractions of strain TL-NPM\* were monitored using oxonol VI and ACMA probes, respectively. Under blue light illumination, the oxonol VI signal indicated an 11.9% increase (suggesting the generation of membrane potential ΔΨ, inside positive), while the ACMA signal showed a 12.9% decrease (suggesting the formation of proton gradient ΔpH, inside acidic) (Fig. 2h, i). However, these induced changes were partially reversed upon treatment with FCCP, an uncoupler for oxidative phosphorylation, leading to a gradual recovery of the oxonol VI and ACMA signals (Fig. 2h, i and Supplementary Fig. 19). These findings demonstrated that NPM\* could convert photons into electrons and incorporate them into the ETC, thereby change the membrane potential and proton gradient. Finally, the intracellular ATP content (C<sub>ATP</sub>) and NADH content (C<sub>NADH</sub>) of strain TL-NPM\* were evaluated. Under blue light illumination, C<sub>ATP</sub> and C<sub>NADH</sub> were found to be 1.85-fold and 1.37-fold higher than those under the dark condition at 15 h and 17 h, respectively (Supplementary Figs. 20–22 and Supplementary Note 7). These results confirmed that the light reaction efficiently converted light energy into metabolic energy in *E. coli*.

To increase the efficiency of light reaction in converting light energy into metabolic energy, improvements were made to both the performance of the ETC and the loading of NPM\* on the IM. Firstly, transcriptomic analysis was performed on strain TL-NPM\* to identify key limiting genes for ATP and NADH generation (Supplementary Fig. 23 and Supplementary Note 8). As a result, *ubiV* (encoding ubiquinone biosynthesis pathway enzyme) and *nadD* (encoding nicotinate-nucleotide adenyltransferase) were selected to enhance the efficiency of ATP and NADH generation, respectively (Supplementary Fig. 24 and Supplementary Note 9). Overexpression of *ubiV* and *nadD* in strain TL-NPM\*-UN led to increases in C<sub>ATP</sub> and C<sub>NADH</sub> by 76.2% and 109.0%, respectively, compared to strain TL-NPM\* under blue light illumination (Fig. 3a, b). To increase NPM\* loading on the IM, the mean cell surface area of strain TL-NPMS\* (11.03 μm<sup>2</sup>) was increased by overexpressing gene *sula*<sup>36</sup> (Supplementary Fig. 25), resulting in a 33.8% increase compared to strain TL-NPM\* (8.24 μm<sup>2</sup>) (Fig. 3c and Supplementary Fig. 26). In addition, the expression of NuoK\* + PufL in strain TL-NPM\* was enhanced using the promoter P<sub>J23119</sub>, generating strain TL-NPM<sup>#</sup>. However, no significant difference was observed in the photocurrents (used to evaluate NPM\* loading) generated by strains TL-NPMS\*, TL-NPM<sup>#</sup>, and TL-NPM\*. To address this issue, the promoter P<sub>J23119</sub> was used to simultaneously enhance the expression of *Sula* and NuoK\* + PufL, generating strain TL-NPMS<sup>#</sup> (Supplementary Fig. 27). The photocurrent generated by strain TL-NPMS<sup>#</sup> (maximum 0.49 μA) was consistently higher than that of strain TL-NPM\* (maximum 0.39 μA) (Fig. 3d), indicating that NPM\* loading was improved by increasing the mean cell surface area and enhancing

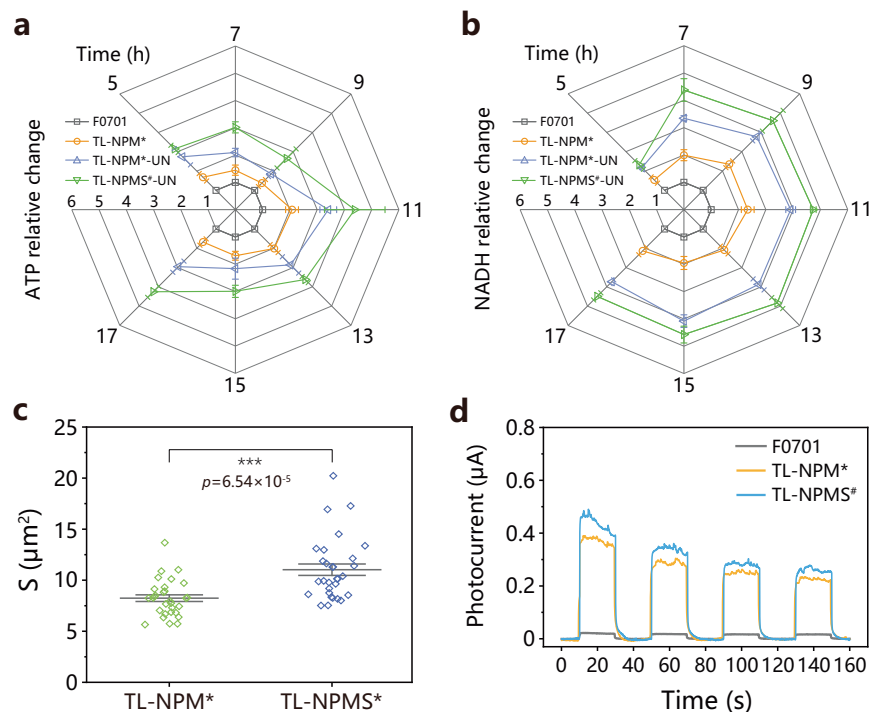


**Fig. 3 | Optimizing the efficiency of light reaction in converting light energy into metabolic energy in *E. coli*.** **a**, **b** The relative change of intracellular ATP (**a**) and NADH (**b**) contents for strains F0701, TL-NPM\*, TL-NPM\*-UN, and TL-NPMS\*<sup>#</sup>-UN under blue light illumination. **c** The mean cell surface area (*S*) of strains TL-NPM\* and TL-NPMS\* were calculated in three different fields (30 cell samples) in microscope images, respectively. **d** The photocurrent generated by strains F0701, TL-

NPM\*, and TL-NPMS\*<sup>#</sup> under xenon lamp illumination ( $\lambda > 400$  nm, turn on 20 s and turn off 20 s for four cycles). Values were shown as mean  $\pm$  s.d. ( $n = 30$  biologically independent replicates (**c**) or three biologically independent replicates (**a**, **b**)). All experiments were repeated independently three times with similar results (**d**). \* $p < 0.05$ , \*\* $p < 0.01$ , \*\*\* $p < 0.001$ , n.s., no significance, as determined by two-sided *t* test. Source data are provided as a Source Data file.

NuoK\* + PufL expression. Finally, the  $C_{ATP}$  and  $C_{NADH}$  of strain TL-NPMS\*<sup>#</sup>-UN (with increased NPM\* loading in strain TL-NPM\*-UN) were increased by 153.9% and 134.2%, respectively, compared to those of strain TL-NPM\* under blue light illumination, and by 337.9% and 383.7% compared to strain F0701 (Fig. 3a, b). These results indicated that the efficiency of the light reaction in converting light energy into metabolic energy was significantly improved by engineering both the ETC and NPM\*.

### Designing and constructing of a dark reaction

To construct a dark reaction in *E. coli* for the synthesis of central metabolites such as pyruvate, a synthetic CO<sub>2</sub>-fixation pathway, named the Artificial Dark Reaction Pathway (ADRP), was developed<sup>29</sup> (Fig. 4a). The ADRP consists of two metabolic modules: (1) the C1 module, responsible for converting CO<sub>2</sub> to formaldehyde; (2) the C3 module, which converts dihydroxyacetone to pyruvate. These modules were connected by formolase (FLS\*), which condense three molecules of formaldehyde into one molecule of dihydroxyacetone. Based on the biochemical reactions collected in the BKMS-react database (<https://bkms.brenda-enzymes.org/>), two distinct C1 module (C1A and C1B) and two distinct C3 module (C3A and C3B) were mined (Supplementary Fig. 28a, b). Thermodynamic analyses were conducted for the four combinations of C1 and C3 module. As shown in Supplementary Fig. 28c, d, the C1A + C3B and C1B + C3B combinations exhibited more favorable standard Gibbs free energies compared to the other combinations. Consequently, the C1A + C3B and C1B + C3B combinations were selected as candidates for the construction of ADRP.

To construct the ADRP in vitro, enzymes from the C1A, C1B, and C3B modules were screened. In the C1A module, two carboxylic acid reductases (niCAR and mmCAR) from *Nocardia iowensis* and *Mycobacterium marinum*, respectively, were unable to catalyze formate to formaldehyde. For the C1B module, acetate kinase (stAckA) from

*Salmonella typhimurium* and aspartate-semialdehyde dehydrogenase (ecASD) from *E. coli* were chosen for the C1B1 and C1B2 reactions, exhibiting the specific activities of 0.067 U/mg and 0.018 U/mg, respectively (Fig. 4b and Supplementary Fig. 29). In the C3B module, methylglyoxal synthase (bsMgsA) from *B. subtilis* and lactaldehyde dehydrogenase (ecLDH) from *E. coli* were selected for the C3B2 and C3B3 reactions, with the specific activities were 0.154 U/mg and 15.59 U/mg, respectively (Fig. 4b and Supplementary Fig. 30). Based on these results, the C1B and C3B modules were assembled to form a complete ADRP, involving six pathway enzymes: formate dehydrogenase (C1FDH), formate reductase (FR, constructed by fusing stAckA and ecASD (Supplementary Fig. 31)), formolase (FLS\*), dihydroxyacetone kinase (scDHAK), methylglyoxal synthase (bsMgsA), and lactaldehyde dehydrogenase (ecLDH) (Fig. 4a). After an 18 h one-pot catalysis, 0.11 g/L pyruvate was detected in the reaction mixture containing all ADRP pathway enzymes, whereas no pyruvate was detected in reaction mixture lacking C1FDH (Fig. 4c–e and Supplementary Fig. 32). These results demonstrated that ADRP was successfully constructed in vitro for CO<sub>2</sub> fixation and the synthesis of central metabolites.

Based on in vitro results, the feasibility of the ADRP was subsequently assessed in vivo. The max-min driving force (MDF) value of the ADRP was approximately 2.76 kJ/mol (Supplementary Fig. 33), indicating thermodynamic feasibility within physiological metabolite concentration ranges. The ADRP was then introduced into strain *E. coli* TD-F0 (strain F0701  $\Delta$ *frmA*) to create strain TD-F1. Using <sup>13</sup>C isotope tracing technology, the relative abundances of intracellular ADRP intermediate metabolites, DHA (m + 3), methylglyoxal (m + 3), and pyruvate (m + 3), were found to be 20.8, 18.4, and 14.9%, respectively. In contrast, these metabolites were below the detection limit in strain TD-F0 (Fig. 4f, g and Supplementary Fig. 34). These results indicated that dark reaction was successfully constructed in vivo, enabling CO<sub>2</sub> fixation for the biosynthesis of central metabolites.

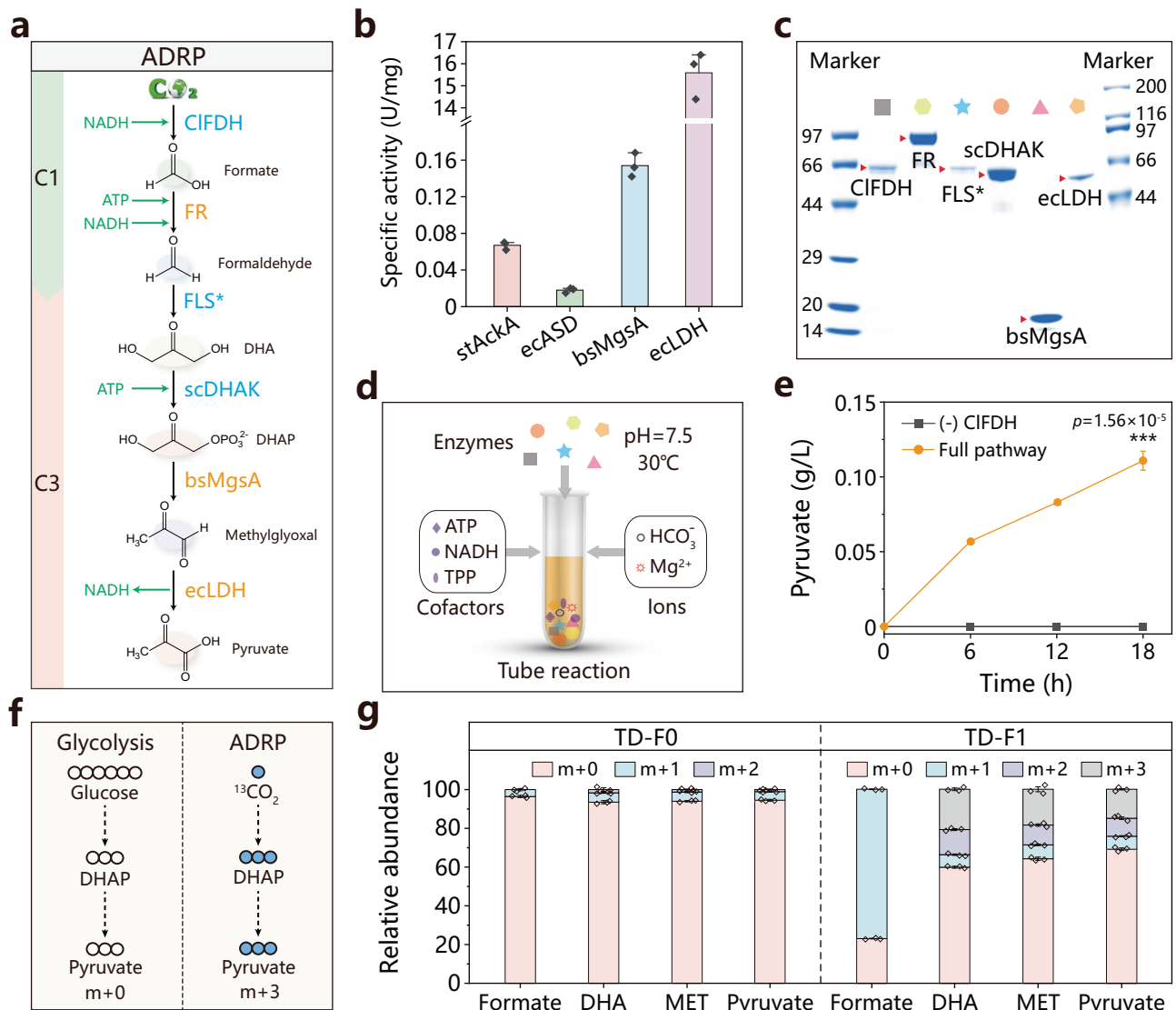


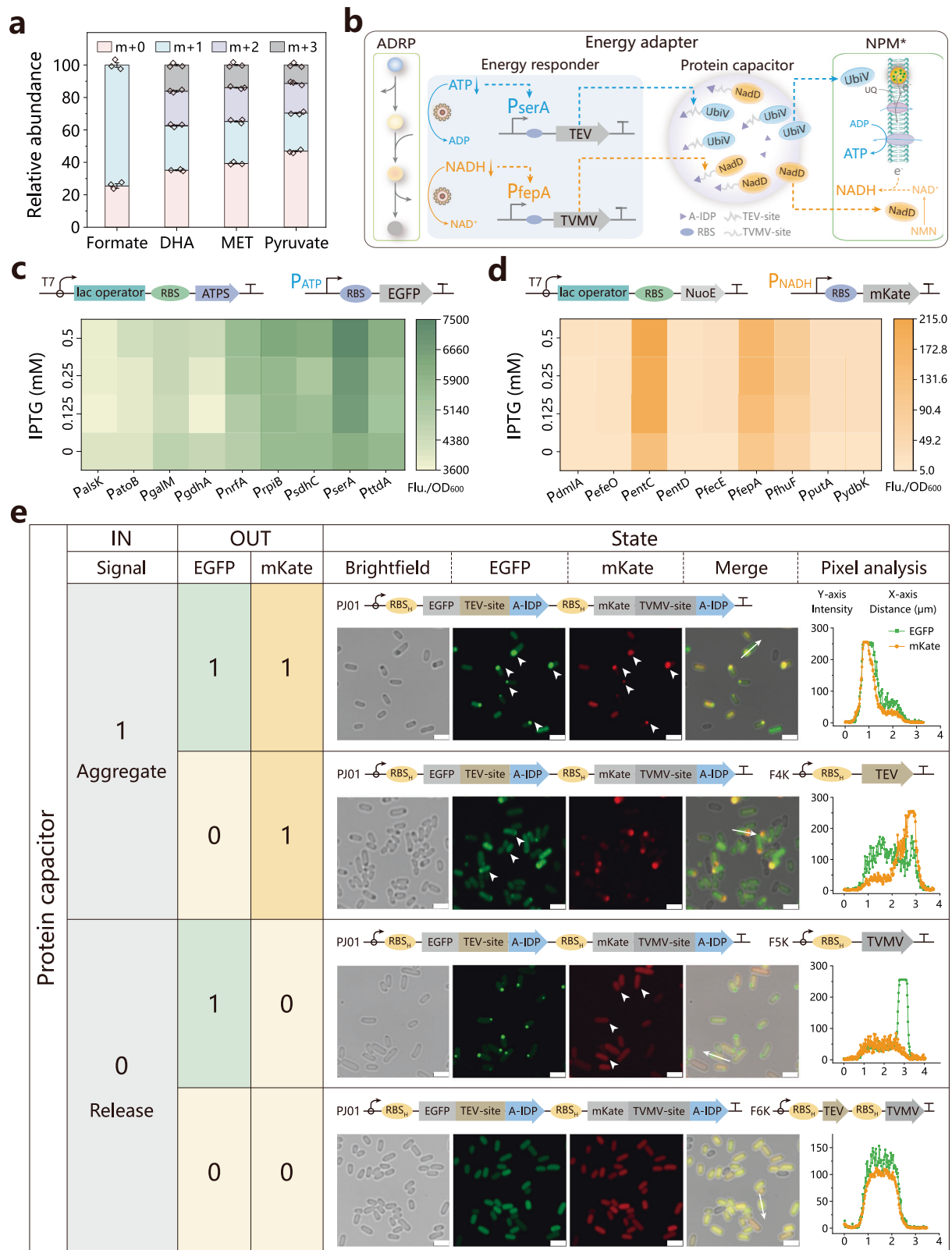
**Fig. 4 | Design and construction of dark reaction in *E. coli*.** **a** Designing a synthetic  $\text{CO}_2$ -fixation pathway-ADRP. Abbreviation: DHA, dihydroxyacetone; DHAP, dihydroxyacetone phosphate; ATP, adenosine triphosphate; NADH, nicotinamide adenine dinucleotide reduced; C1, C1 module; C3, C3 module; ADRP, artificial dark reaction pathway. **b** The specific activity of stAckA, ecASD, bsMgsA, and ecLDH. **c** SDS-PAGE of purified enzymes (C1FDH, FR, FLS\*, scDHAK, bsMgsA, and ecLDH) in ADRP. The unit is kDa. **d** Schematic diagram of ADRP reconstruction in vitro for one-pot catalysis. Abbreviation: ATP, adenosine triphosphate; NADH, nicotinamide adenine dinucleotide reduced; TPP, thiamine pyrophosphate. **e** Time curve of pyruvate accumulation in reaction supernatant with full ADRP enzymes and the control without C1FDH. **f** Schematic diagram of carbon atoms transit to pyruvate via glycolysis pathway and ADRP. The labeled ( $^{13}\text{C}$ ) and unlabeled carbon atoms were represented by closed and open circles, respectively. **m** + 0 represents metabolites

without  $^{13}\text{C}$  atom and **m** + 3 represents metabolites with three  $^{13}\text{C}$  atoms. Abbreviation: DHAP, dihydroxyacetone phosphate. **g** Relative abundance of mass isotopomers for intracellular formate, DHA, MET, and pyruvate in strains TD-F0 and TD-F1 under 24 h anaerobic fermentation ( $\text{NaH}^{13}\text{CO}_3$  and glucose were used as co-substrates; 5 mM ATP, 5 mM NADH, and glucose were exogenously added to medium to provide additional metabolic energy in this experiment). **m** + 0 represented metabolites without  $^{13}\text{C}$  atom, **m** + 1 represented metabolites with one  $^{13}\text{C}$  atom, **m** + 2 represented metabolites with two  $^{13}\text{C}$  atoms, and **m** + 3 represented metabolites with three  $^{13}\text{C}$  atoms. Abbreviation: DHA, dihydroxyacetone; MET, methylglyoxal. Values were shown as mean  $\pm$  s.d. from three biological replicates (**b**, **e**, **g**). All experiments were repeated independently three times with similar results (**c**). \* $p$  < 0.05, \*\* $p$  < 0.01, \*\*\* $p$  < 0.001, n.s., no significance, as determined by two-sided  $t$  test. Source data are provided as a Source Data file.

### Constructing and adapting photosynthesis system

To construct a photosynthesis system, the light and dark reactions were integrated into *E. coli*, generating strain TC-F1. Under blue light illumination, the relative abundances of ADRP intermediate metabolites in strain TC-F1, including formate (**m** + 1), DHA (**m** + 3), methylglyoxal (**m** + 3), and pyruvate (**m** + 3), were found to be 74.6, 16.2, 14.0, and 11.4%, respectively (Fig. 5a). In contrast, in the absence of blue light illumination, the relative abundance of formate (**m** + 1) in strain TC-F1 was 63.6%, while pyruvate (**m** + 3) was below the detection limit (Supplementary Figs. 35, 36). These results indicated that the photosynthesis system was successfully constructed in *E. coli*.

To dynamically match the light reaction with the dark reaction, an energy adapter consisting of an energy responder and a protein capacitor was developed (Fig. 5b). The energy responder expressed TEV and TVMV proteases<sup>37</sup> through the  $P_{\text{serA}}$  and  $P_{\text{repA}}$  promoters, which could sense decreases in intracellular ATP and NADH levels, respectively. The protein capacitor expressed fusion proteins, UbiV + TEV-site + A-IDP and NadD + TVMV-site + A-IDP, formed by combining the protein phase-separation element A-IDP (artificially intrinsically disordered protein)<sup>38</sup>, the recognition site for TEV and TVMV, and the regulatory proteins UbiV and NadD. The operational principle of the energy adapter can be described as follows: (1) In standby mode, the



energy responder remains inactive while the protein capacitor performed charging, causing UbiV + TEV-site + A-IDP and NadD + TVMV-site + A-IDP to pre-aggregate into a protein droplet, thereby limiting their function. (2) In running mode, the activation of the energy responder leads to the generation of TEV and TVMV proteases, which then remove the A-IDP element from the fusion proteins. Consequently, the protein capacitor performed discharging, releasing UbiV

and NadD to perform their functions. In summary, this dynamic energy adapter was used to enhance the compatibility between the light and dark reactions by sensing the energy demand of the dark reaction and supplying this demand through the light reaction.

To build an energy responder, transcriptome analysis was performed on the energy-deficient strains TC-E1 and TC-E2 (Supplementary Fig. 37 and Supplementary Note 10) to identify promoters that

**Fig. 5 | Construction of *E. coli* photosynthesis system with an energy adapter.**

**a** Relative abundance of mass isotopomers for intracellular formate, DHA, MET, and pyruvate in strain TC-F1 with blue light illumination. Abbreviation: DHA, dihydroxyacetone; MET, methylglyoxal. **b** Schematic diagram of *E. coli* photosynthesis system with an energy adapter to dynamically match light reaction (NPM\*) and dark reaction (ADRP). Abbreviation: ATP/ADP, adenosine triphosphate/diphosphate; NADH/NAD<sup>+</sup>, nicotinamide adenine dinucleotide reduced/oxidized; P<sub>serA</sub>, promoter serA; P<sub>fepA</sub>, promoter fepA; TEV, tobacco etch virus protease; TVMV, tobacco vein mottling virus protease; A-IDP, artificial intrinsically disordered protein; RBS, ribosome binding site; TEV-site, TEV recognition site; TVMV-site, TVMV recognition site; UQ, ubiquinone; NMN, nicotinamide mononucleotide; e<sup>-</sup>, electron. **c, d** The effectiveness of nine candidate promoters in sensing ATP levels (**c**) and NADH levels (**d**) was evaluated by detecting EGFP (IPTG induction for 4 h) and mKate (IPTG induction for 2 h) fluorescence intensity, respectively. IPTG could induce the expression of ATPS and NuoE to consume ATP and NADH, thereby decreasing the intracellular ATP and NADH levels. Gradient concentrations of IPTG

were added to generate different intracellular ATP and NADH levels. Abbreviation: T7, T7 promoter; IPTG, isopropyl-β-D-thiogalactopyranoside; ATPS, ATP sulfurylase; NuoE, NADH dehydrogenase complex subunit E; P<sub>ATP</sub>, promoter that senses intracellular ATP levels; P<sub>NADH</sub>, promoter that senses intracellular NADH levels; EGFP, enhanced green fluorescent protein; mKate, a basic red fluorescent protein. **e** The effectiveness of the protein capacitor was evaluated by laser confocal microscopy images and pixel intensity analysis. 1 and 0 signals represented the aggregation and release of protein, respectively. (1, 1), (0, 1), (1, 0), and (0, 0) represented the four states of protein capacitor. The white scale bar at the bottom right of the microscope image represented 2.5 μm. The pixel intensity data was collected by laser confocal microscopy software LAS AF Lite along the track of a white solid arrow in the microscope image. Cells pointed by white triangular arrows had significant differences in microscope images. Abbreviation: RBS<sub>H</sub>, high strength ribosome binding site. Values were shown as mean ± s.d. from three biological replicates (**a, c, d**). All experiments were repeated independently three times with similar results (**e**). Source data are provided as a Source Data file.

could respond to decreases in intracellular ATP and NADH levels, respectively. Based on transcriptomic analysis (Supplementary Fig. 38 and Supplementary Note 11), the effectiveness of these candidate promoters was evaluated using EGFP and mKate as reporter genes (Fig. 5c, d). As a result, the P<sub>serA</sub>, P<sub>sdhC</sub>, and P<sub>rpiB</sub> promoters were identified as responsive to the decrease of intracellular ATP levels, exhibiting increases in EGFP fluorescence intensity of 21.4%, 7.6%, and 9.6%, compared to the control strain (Fig. 5c). In addition, the P<sub>encC</sub> and P<sub>fepA</sub> promoters were found to respond to decreases in intracellular NADH levels, displaying increases in mKate fluorescence intensity of 55.2% and 62.7%, respectively, compared to the control strain (Fig. 5d). Therefore, the P<sub>serA</sub> and P<sub>fepA</sub> promoters were selected for constructing the energy adapter.

To construct a protein capacitor, fusion proteins EGFP + TEV-site + A-IDP and mKate + TVMV-site + A-IDP were generated and expressed. Fluorescence microscope images and pixel intensity analysis showed that EGFP and mKate could undergo phase-separate to form protein droplets or be released into the cytoplasm simultaneously (Fig. 5e and Supplementary Fig. 39). These results indicated that the protein capacitor could effectively aggregate or release both proteins simultaneously. When TEV or TVMV protease was independently expressed, EGFP or mKate was released separately and distributed evenly in the cytoplasm, while the other protein remained aggregated in droplets (Fig. 5e). This indicates the protein capacitor can selectively release individual proteins from the protein droplet. In conclusion, the protein capacitor was successfully constructed to facilitate the aggregation and release of two proteins.

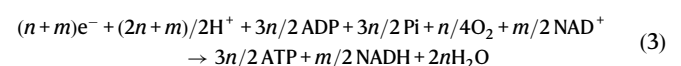
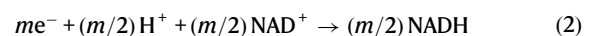
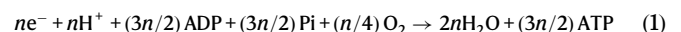
To construct an energy adapter, an energy responder and a protein capacitor were assembled (Fig. 5b). The effectiveness of the energy adapter was validated using EGFP and mKate by constructing fusion proteins UbiV + EGFP + TEV-site + A-IDP and NadD + mKate + TVMV-site + A-IDP (Fig. 6a, d). In standby mode, the energy responder remained inactive, and the charging process of the protein capacitor was evaluated at three distinct levels: low, medium, and high levels (Supplementary Fig. 40). As a result, the average EGFP pixel intensities for the low, medium, and high charging levels were approximately -125, -135, and -170, respectively, while the average mKate pixel intensities were around -75, -160, and -185, respectively (Fig. 6c, f and Supplementary Figs. 41c, f and 42c, f). In running mode, the energy responder was activated, and the discharging process of the protein capacitor was evaluated based on two criteria: an increase in cytoplasmic average pixel intensity (CAPI) and a decrease in droplet average pixel intensity (DAPI). When a low level of charging was applied, strains TC-AA1 (harboring plasmids PJO1-CL, pCDR-ST, and pET28a-ATPS) and TC-ANI (harboring plasmids PJO1-CL, pCDR-FT, and pET28a-NuoE) exhibited a 203.1% and 690.8% increase in CAPI, along with a 29.8% and 100.0% decrease in DAPI, respectively, compared to the inactive energy responder (Fig. 6b, c and e, f). However, at medium and high charging levels, the changes in

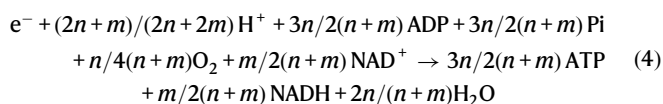
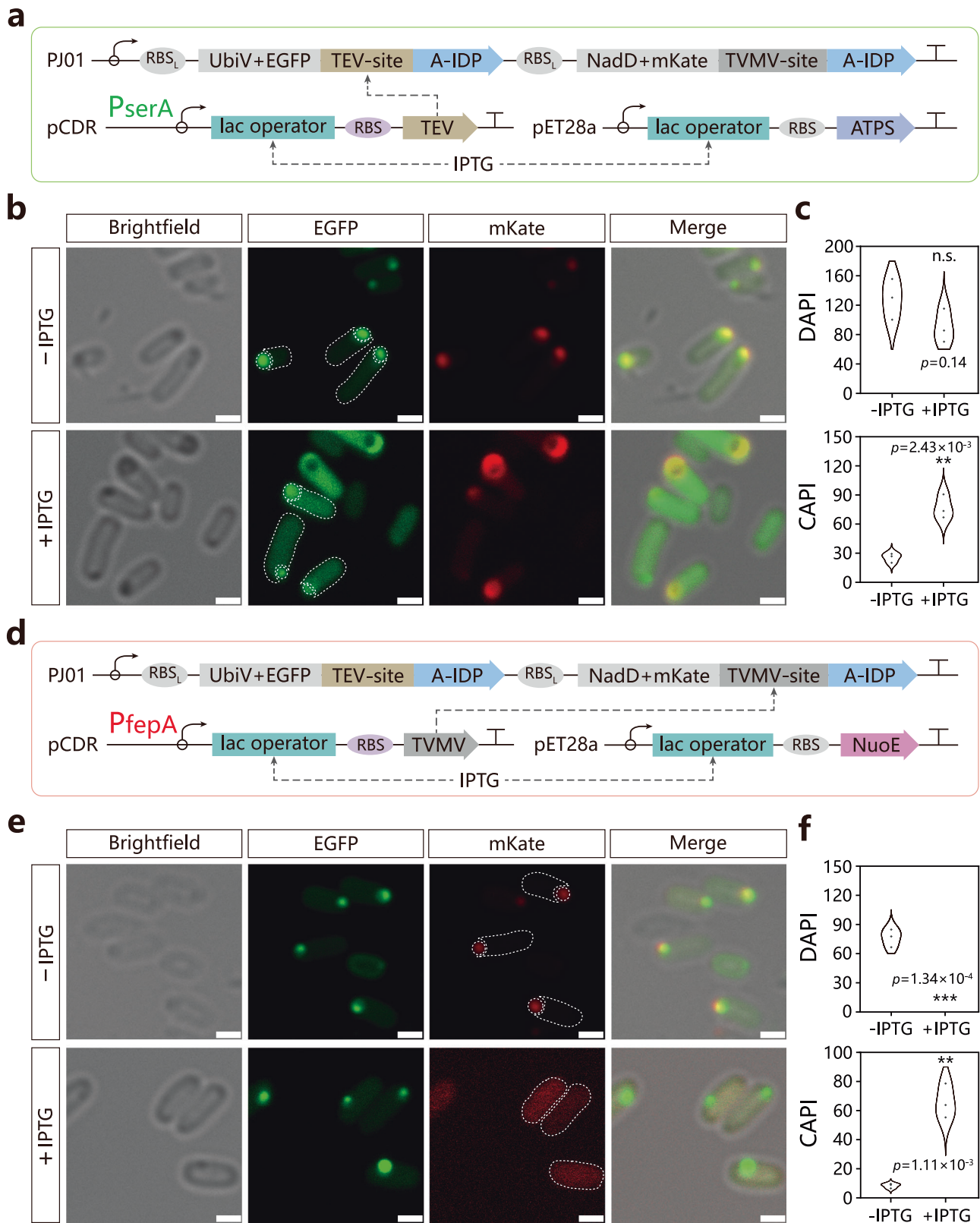
CAPI and DAPI did not meet the expected criteria (Supplementary Figs. 41, 42). Therefore, a low level of charging was found to be most effective for the operation of the energy adapter in both standby and running modes. In conclusion, an energy adapter was successfully developed to dynamically match the light and dark reactions.

**Programming photosynthesis system for diverse bioproduction**

To enable diverse bioproduction of the photosynthesis system, the electron distribution of the light reaction can be programmed into three distinct modes using the energy adapter: (1) ATP and NADH-unbiased distribution mode (UDM), where photogenerated electrons are distributed to generate equal equivalents of ATP and NADH; (2) NADH-biased distribution mode (NBDM), where photogenerated electrons are preferentially directed to generate more equivalents of NADH than ATP; (3) ATP-biased distribution mode (ABDM), where photogenerated electrons are preferentially directed to generate more equivalents of ATP than NADH (Fig. 7a, b).

To achieve these three distribution modes, the electron distribution in the light reaction was theoretically analyzed. It was assumed that the electron equivalent contributing to the generation of ATP and NADH is represented by  $n$  ( $n > 0$ ) and  $m$  ( $m > 0$ ), respectively. The electron distribution index between ATP and NADH generation is denoted by  $p$  ( $p = n/m$ ,  $p > 0$ ). Additionally, the equivalent of ATP and NADH generation was defined as  $N_{ATP}$  ( $N_{ATP} > 0$ ) and  $N_{NADH}$  ( $N_{NADH} > 0$ ), respectively. The energy supply index between ATP and NADH equivalent in the light reaction was represented by ESI ( $ESI = N_{ATP}/N_{NADH}$ ,  $ESI > 0$ ). Through calculations outlined in Supplementary Note 12, Eqs. (1) and (2) were derived, leading to Eq. (3) by summing the two. This showed that one equivalent of the electron could be converted into  $N_{ATP} = 3n/2(n+m)$  and  $N_{NADH} = m/2(n+m)$  in Eq. (4). Based on this analysis, it was concluded that when the photogenerated electron distribution is set to ABDM,  $ESI = N_{ATP}/N_{NADH} > 1$  ( $p > 1/3$ ,  $n > m/3$ ); when set to UDM,  $ESI = N_{ATP}/N_{NADH} = 1$  ( $p = 1/3$ ,  $n = m/3$ ); and when set to NBDM,  $ESI = N_{ATP}/N_{NADH} < 1$  ( $0 < p < 1/3$ ,  $0 < n < m/3$ ) (Fig. 7b). These hypotheses were validated by introducing protein capacitor with different discharging regulators into strain TL-NPMS<sup>#</sup> (generating a series of strains TP-1 - TP-9), respectively (Supplementary Fig. 43 and Supplementary Note 13). These results indicated that the photosynthesis system in *E. coli* could be programmed to operate in three modes: ABDM, UDM, and NBDM.





To enable the programmable photosynthesis system to utilize one-carbon substrates, the iPBRC strategy was developed by integrating the photosynthetic building (PB) stage and resting catalytic (RC) stage

to produce different biofuels and biochemicals (Fig. 7c). Firstly, the ratio of theoretical ATP equivalent to NADH equivalent consumed by the biosynthetic pathway for bioproduction was defined as energy demand index (EDI). It was observed that the EDI in the ADRP-based pathway for acetone, malate, and  $\alpha$ -ketoglutarate ( $\alpha$ -KG) biosynthesis were  $8/8=1$ ,  $5/6 < 1$ , and  $5/4 > 1$  (Supplementary Note 14), which could be matched with  $ESI=1$ ,  $< 1$ , and  $> 1$ , respectively. As proof of concept, when the programmable photosynthesis system was switched to UDM,

**Fig. 6 | Construction and evaluation of energy adapter in *E. coli*.** **a** Constructing energy adapter by assembling the  $P_{serA}$  promoter-based energy responder and the regulatory protein (UbiV and NadD)-based protein capacitor with a low degree of charging. Abbreviation: RBS<sub>L</sub>, low strength ribosome binding site; EGFP, enhanced green fluorescent protein; mKate, a basic red fluorescent protein; TEV-site, TEV recognition site; TVMV-site, TVMV recognition site; A-IDP, artificial intrinsically disordered protein;  $P_{serA}$ , promoter serA; RBS, ribosome binding site; TEV, tobacco etch virus protease; ATPS, ATP sulfurylase; IPTG, isopropyl- $\beta$ -D-thiogalactopyranoside. **b, c** Laser confocal microscopy images and pixel intensity analysis to verify the effectiveness of an energy adapter that senses and regulates the intracellular ATP levels in standby and running modes. **d** Constructing energy adapter by assembling the  $P_{fepA}$  promoter-based energy responder and the regulatory protein (UbiV and NadD)-based protein capacitor with a low degree of

charging. Abbreviation:  $P_{fepA}$ , promoter fepA; TVMV, tobacco vein mottling virus protease; NuoE, NADH dehydrogenase complex subunit E. **e, f** Laser confocal microscopy images and pixel intensity analysis to verify the effectiveness of energy adapter that senses and regulates the intracellular NADH levels in standby and running modes. The white scale bar at the bottom right of the microscope image represented 1.0  $\mu$ m (**b, e**). The average pixel intensity data within the white dashed circle was collected by software Image J in microscope image (**b, e**). The white dashed circles represented the outlines of the cytoplasmic region and droplet region in the microscope image, respectively (**b, e**). Values were shown as mean  $\pm$  s.d. from three biological replicates (**c, f**). All experiments were repeated independently three times with similar results (**b, e**). \* $p < 0.05$ , \*\* $p < 0.01$ , \*\*\* $p < 0.001$ , n.s., no significance, as determined by two-sided  $t$  test. Source data are provided as a Source Data file.

NBDM, and ABDM, the production of acetone with strain TP-A (Supplementary Figs. 44–46), malate with strain TP-M (Supplementary Figs. 47, 48), and  $\alpha$ -KG with strain TP-K (Supplementary Figs. 49, 50) reached at 10.47 g/L, 24.71 g/L, and 15.25 g/L, respectively, representing increases of 22.5, 34.3, and 21.1% compared to strains TP-A0, TP-M0, and TP-K0, respectively (Fig. 7d and Supplementary Figs. 51, 52). These results demonstrated that the energy adapter significantly enhances the production performance of the photosynthesis system. Furthermore, the CO<sub>2</sub> utilization rates (with one equivalent of methanol equated to one equivalent of CO<sub>2</sub>, Supplementary Notes 15, 16) for strains TP-A, TP-M, and TP-K were up to 52.69 mg/gDCW/h, 71.96 mg/gDCW/h, and 50.65 mg/gDCW/h, respectively (Fig. 7e, f). In this case, the solar-to-chemical energy efficiencies of this system to produce acetone, malate, and  $\alpha$ -KG were estimated to be 1.14%, 0.36%, and 0.13%, respectively (Supplementary Note 17). Finally, the production of acetone, malate, and  $\alpha$ -KG reached at 17.46 g/L, 33.76 g/L, and 23.39 g/L in a 5 L bioreactor, respectively (Fig. 7g). Through the iPBC strategy, it was estimated that 0.23 to 0.84 tCO<sub>2</sub> could be stored in 1 ton of target products, resulting in a negative carbon footprint of  $-0.84$  kgCO<sub>2</sub>e/kg acetone,  $-0.34$  kgCO<sub>2</sub>e/kg malate, and  $-0.23$  kgCO<sub>2</sub>e/kg  $\alpha$ -KG (Fig. 7h, i). These results highlight the capability of the programmable photosynthesis system for carbon storage and carbon-negative biomanufacturing.

### Optimizing photosynthesis system for one-carbon trophic growth

To achieve light-driven one-carbon trophic growth, the optimization of the dark reaction in the photosynthesis system and adaptive laboratory evolution were performed (Fig. 8a). Firstly, the carbon flux within the C3 module of the dark reaction in strain TC-F1, which harbors the photosynthesis system, was enhanced by overexpressing FLS\* through the introduction of plasmid pCDR-FLS\*, resulting in strain TC-F2. Secondly, the carbon flux of the C1 module was further increased by the exogenous addition of formate. In NBS medium containing 100 mM NaHCO<sub>3</sub> (equivalent to CO<sub>2</sub>), 200 mM methanol, 200 mM formate, and 50 mM glucose (NBS-CMFG), strain TC-F2 achieved an optical density at 600 nm (OD<sub>600</sub>) of 3.19 (Fig. 8b). Thirdly, a long-term evolutionary process was employed to convert strain TC-F2 into a light-driven one-carbon trophic *E. coli*, this process involved gradually reducing the glucose concentration from 50 mM to 0 mM in the feed medium to intensify the evolutionary pressure. After 110 days of evolution, strain TC-F3 was capable of growing using NaHCO<sub>3</sub> (22.78 mM), methanol (47.48 mM), and formate (27.14 mM) as carbon sources, achieving an OD<sub>600</sub> value of 0.417 and a doubling time of 19.86 h (Fig. 8b, c). Finally, the labeling pattern of proteinogenic amino acids was analyzed through <sup>13</sup>C labeling experiments, which confirmed that all biomass building blocks were derived from one-carbon substrates (NaHCO<sub>3</sub>, methanol, and formate). When fed with <sup>13</sup>C-NaHCO<sub>3</sub>, <sup>13</sup>C-methanol, and <sup>13</sup>C-formate, nearly all relevant amino acids were labeled, with the total fraction of labeled carbon reaching 99.3% (Fig. 8d). These findings indicated that the light-driven one-carbon

trophic growth of *E. coli* utilized a new-to-nature photosynthesis system, with biomass carbon derived from one-carbon substrates.

### Discussion

In this study, a new-to-nature photosynthesis system was engineered to utilize one-carbon substrates. Firstly, a tailored light reaction was constructed to convert light energy into ATP and NADH, by constructing a biogenic photosystem NPM\*. Secondly, a sustainable photosynthesis system was established for the synthesis of key central metabolites, such as pyruvate, by integrating the light and dark reactions to utilize one-carbon substrates. Finally, a programmable photosynthesis system was implemented by installing an energy adapter to enable the production of different chemicals, such as acetone, malate, and  $\alpha$ -ketoglutarate, with a negative carbon footprint. This system was further optimized to achieve light-driven one-carbon trophic growth. Although a promising proof of concept remains incomparable to natural photosynthetic bacteria, this system provides new insights into the development of fully photoautotrophic *E. coli* cell factories capable of producing value-added bioproducts in the future.

The tailored light reaction equips heterotrophic microbial cells with the ability to convert light energy into metabolic energy. Recently, three classical photosystems have been developed: (i) the natural photosystem in photoautotrophic microbes (e.g., cyanobacterial and microalgae)<sup>39,40</sup>; (ii) the light-powered proton pump PR<sup>41,42</sup>; (iii) photosensitive electron-source nanomaterials<sup>14,18</sup>. While the natural photosystem has been modified to enhance the performance of photoautotrophic microbes, further improvements are required to optimize their productivity of industrial applications<sup>10,43</sup>. Conversely, non-natural photosystems have been widely used to enhance the efficiency of microbial cell factories, but the challenges, such as photosensitizer biotoxicity and the biotic-abiotic interface effects remain significant obstacles to their advancement<sup>20,28</sup>. In our study, the light reaction was developed by restructuring the photosystem of photosynthetic bacteria, which exhibited excellent biocompatibility due to its biologically derived components. Moreover, NPM\* in the light reaction was integrated into the ETC-harboring IM using the transmembrane mechanism of NuoK, which not only was bio-friendly to host cells but also improved the kinetics of electron transfer. Consequently, the electrons generated by NPM\* were capable of regenerating NADH and contributing to the establishment of a proton gradient to drive ATP synthesis. However, potential toxicity from MgP under increased light intensity may limit the efficiency of light reactions. Future efforts should focus on the development of intelligent light intensity control circuits, which combining biosensors and real-time photosource devices, and the construction of intracellular detoxification modules by enhancing superoxide dismutase expression to overcome these limitations. In addition, establishing a standard operating procedure (SOP) for NPM\*, including standardizing ETC performance and NPM\* loading, will be crucial for constructing an efficient light reaction through iterative rounds of the Design-Build-Test-Learn cycle<sup>44</sup>. Furthermore, exploring the interaction between

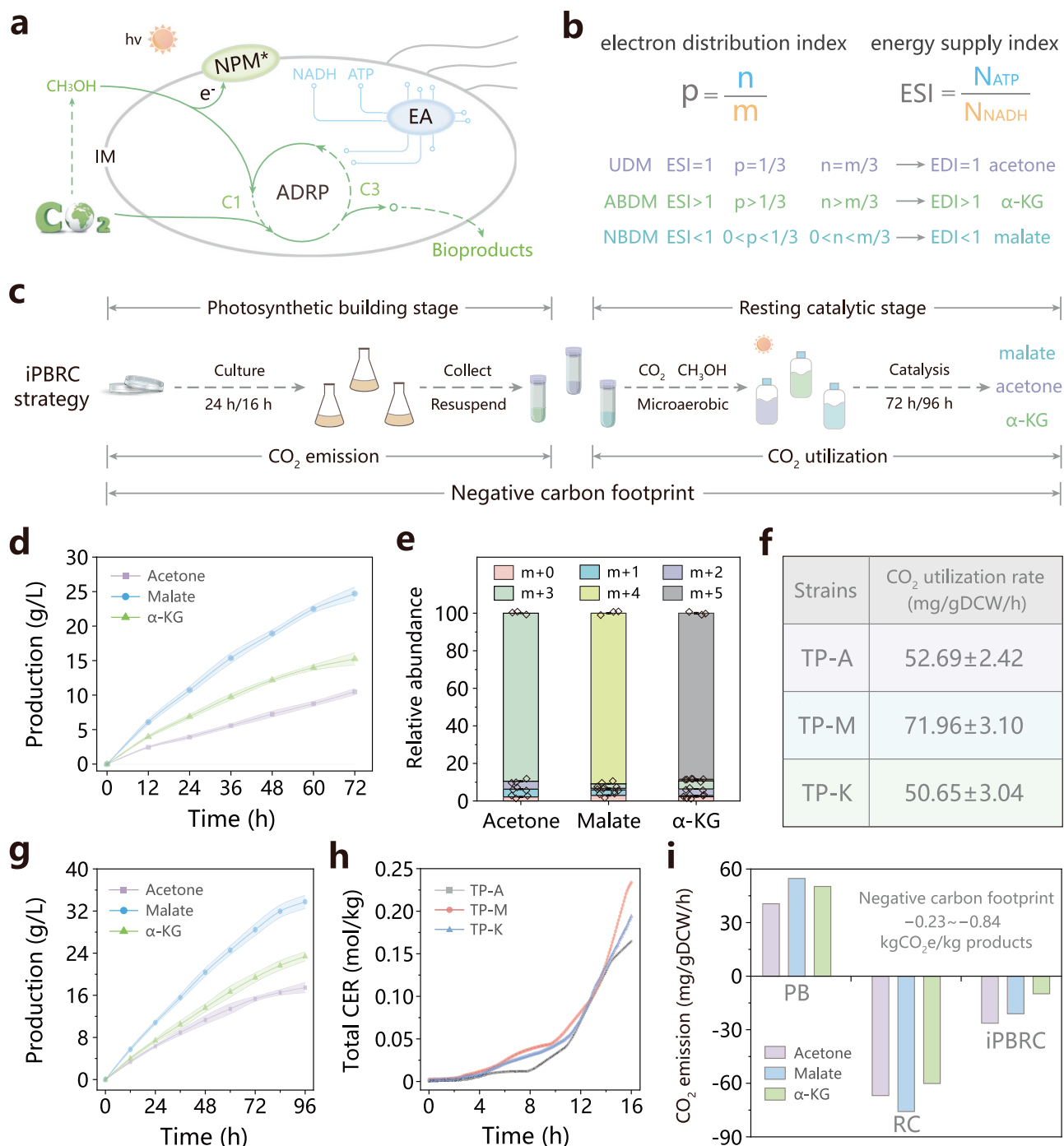


**Fig. 7 | Programming *E. coli* photosynthesis system for diverse bioproduction.**

**a** Programming photosynthesis system via energy adapter for one-carbon substrates utilization. Abbreviation: hv, photon energy; e<sup>-</sup>, electron; NPM\*, photosystem Nuok\* + PufL + MgP; CO<sub>2</sub>, carbon dioxide; CH<sub>3</sub>OH, methanol; ATP, adenosine triphosphate; NADH, nicotinamide adenine dinucleotide reduced; ADRP, artificial dark reaction pathway; C1, C1 module; C3, C3 module; IM, inner membrane; EA, energy adapter. **b** The definition of electron distribution index and energy supply index, and the theoretical analysis of three distribution modes (UDM, ABDM, and NBDM). Abbreviation: ESI, energy supply index; EDI, energy demand index; ABDM, ATP-biased distribution mode; UDM, ATP, and NADH-unbiased distribution mode; NBDM, NADH-biased distribution mode;  $\alpha$ -KG,  $\alpha$ -ketoglutarate. **c** iPBRC strategy enabling a programmable photosynthesis system for one-carbon substrates utilization. **d** The production of acetone, malate, and  $\alpha$ -

KG with a programmable photosynthesis system in strains TP-A, TP-M, and TP-K using the iPBRC strategy at the 200 mL serum bottle scale, respectively. **e** Relative abundance of mass isotopomers for acetone, malate, and  $\alpha$ -KG in the supernatant of the catalytic mixture at 72 h. NaH<sup>13</sup>CO<sub>3</sub> and <sup>13</sup>CH<sub>3</sub>OH were used for <sup>13</sup>C-labeling analysis. **f** The CO<sub>2</sub> utilization rates of strains TP-A, TP-M, and TP-K for the production of acetone, malate, and  $\alpha$ -KG. **g** The production of acetone, malate, and  $\alpha$ -KG with a programmable photosynthesis system in strains TP-A, TP-M, and TP-K using iPBRC strategy in a 5 L bioreactor, respectively. **h** Total CO<sub>2</sub> emission rate (CER) of strains TP-A, TP-M, and TP-K during the photosynthetic building stage, respectively. **i** The CO<sub>2</sub> emissions and negative carbon footprint of acetone, malate, and  $\alpha$ -KG production by iPBRC strategy, respectively. PB, photosynthetic building stage; RC, resting catalytic stage. Values were shown as mean  $\pm$  s.d. from three biological replicates (**d–g**). Source data are provided as a Source Data file.

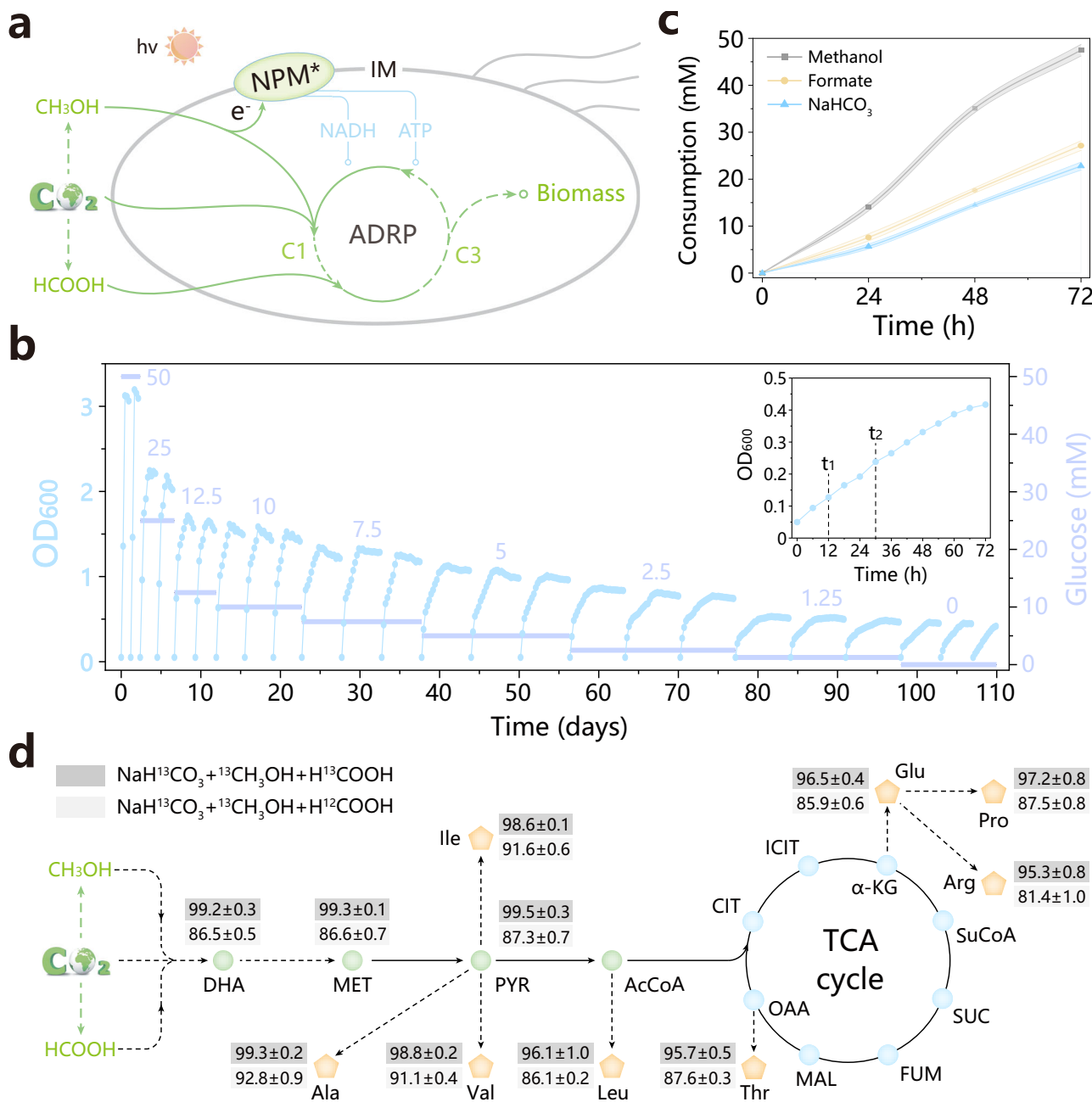


**Fig. 8 | Light-driven one-carbon trophic growth of *E. coli*.** **a** Optimizing photosynthesis system to achieve light-driven one-carbon trophic growth. Abbreviation:  $h\nu$ , photon energy;  $e^-$ , electron; NPM\*, photosystem  $\text{NuoK}^* + \text{PufL} + \text{MgP}$ ;  $\text{CO}_2$ , carbon dioxide;  $\text{CH}_3\text{OH}$ , methanol;  $\text{HCOOH}$ , formate; ATP, adenosine triphosphate; NADH, nicotinamide adenine dinucleotide reduced; ADRP, artificial dark reaction pathway; C1, C1 module; C3, C3 module; IM, inner membrane. **b** The evolution trajectory of strain TC-F3. The OD<sub>600</sub> of representative evolved strains by gradually decreasing glucose concentration from 50 mM to 0 mM. The  $t_1$  and  $t_2$  were used to calculate the doubling time of strain TC-F3 according to the equation in Supplementary Fig. 52. **c** The consumption of methanol, formate, and  $\text{NaHCO}_3$  for strain

TC-F3, respectively. **d** Labeling pattern of proteinogenic amino acids on feeding with  $\text{NaH}^{13}\text{CO}_3 + {}^{13}\text{CH}_3\text{OH} + \text{H}^{13}\text{COOH}$  and  $\text{NaH}^{13}\text{CO}_3 + {}^{13}\text{CH}_3\text{OH} + \text{H}^{12}\text{COOH}$ , respectively. Abbreviation:  $\text{CO}_2$ , carbon dioxide;  $\text{CH}_3\text{OH}$ , methanol;  $\text{HCOOH}$ , formate; DHA, dihydroxyacetone; MET, methylglyoxal; PYR, pyruvate; AcCoA, acetyl-CoA; CIT, citrate; ICIT, isocitrate;  $\alpha$ -KG,  $\alpha$ -ketoglutarate; SuCoA, succinyl-CoA; SUC, succinate; FUM, fumarate; MAL, malate; OAA, oxaloacetate; Ala, alanine; Ile, isoleucine; Val, valine; Leu, leucine; Thr, threonine; Glu, glutamate; Pro, proline; Arg, arginine. Values were shown as mean  $\pm$  s.d. from three biological replicates (**c**, **d**). Source data are provided as a Source Data file.

native energy metabolism and the tailored light reaction is essential. Understanding the process and mechanism of incorporating photo-generated electrons into the native ETC will facilitate the development of strategies to minimize transfer losses of photogenerated electrons. Lastly, optimal strategies, such as assembling light-harvesting antennas onto NPM\* to expand its three-dimensional

structure, will be critical to achieving a more efficient new-to-nature photosystem.

A sustainable photosynthesis system serves as a carbon sink, enabling the utilization of one-carbon substrates with light energy. Currently, two types of NPS have been developed: (i) hemi-NPS, such as the Co-Pi-formate dehydrogenase (FDH) system<sup>45</sup> and *Moorella*

*thermoacetica*/gold nanoclusters biohybrid system<sup>46</sup>; (ii) holo-NPS, such as the chloroplast mimic system (encapsulating photosynthetic membranes and CETCH cycle in droplets)<sup>47</sup> and the cyanobacterial/yeast endosymbiotic system<sup>33</sup>. Although these NPS have been utilized for CO<sub>2</sub> fixation in cell growth and bioproduction, they exhibit several limitations: (i) hemi-NPS assembled in vitro lack the self-replication capability required for large-scale application; (ii) the continuous replication of whole-cell biocatalysts reduces the ratio of semiconductor material to biomass due to the absence of self-regeneration<sup>28</sup>; and (iii) while the endosymbiotic system can enhance yeast growth through bioenergetic functions, its stability requires improvement for biosynthesis applications. In our study, a photosynthesis system was constructed in *E. coli* by coupling two bioheritable components: the light reaction and the dark reaction, demonstrating self-replication and sustainable bioproduction. This engineered *E. coli* with a sustainable photosynthesis system effectively utilized one-carbon substrates, laying a solid foundation for achieving carbon-negative biomanufacturing. Furthermore, compared to the previous iPRCC strategy<sup>7</sup>, the iPBRCC strategy developed in this study offers unique advantages, including the ability to achieve photosynthesis and resting catalysis in an engineered strain, along with a broader capability for one-carbon substrate utilization. In the future, as part of the synthetic biology toolbox, the sustainable photosynthesis system can be engineered and adapted to different application scenarios with enhanced universality and stability. In addition, this sustainable NPS will serve as a novel model for transforming non-photosynthetic microbes into fully photoautotrophic microbes. To achieve this ambitious goal, several challenges must be addressed: (i) enhancing the efficiency of light energy harvesting and conversion for the tailored photosystem; (ii) improving the biosynthesis efficiency of the dark reaction ADRP to support cell growth by optimizing metabolic carbon flux; (iii) establishing an SOP for regulating and optimizing the global metabolic network of the NPS. To overcome these obstacles, efforts will focus on exploring more effective strategies, such as designing specialized photobioreactors to mitigate shading effect during high-density cultivation, developing light-harvesting antennas, reducing transfer losses of photogenerated electrons in the ETC, engineering key enzymes in the ADRP pathway, alleviating formaldehyde-induced DNA-protein crosslinking<sup>48</sup>, and enhancing the overall performance of the NPS through metabolic network model prediction and multi-omics joint analysis.

A programmable photosynthesis system in *E. coli* enables versatile bioproduction by installing an energy adapter to customize the distribution of photogenerated electrons. Although NPS have been widely used in chemical synthesis, two major limitations have hindered their broader application: (i) NPS have predominantly been used to synthesize simple products, such as formate<sup>45</sup> and acetate<sup>46</sup> from CO<sub>2</sub>, without extending to the production of longer carbon-chain and more diverse compounds<sup>28</sup>; (ii) while NPS have been employed to enhance biosynthetic efficiency through the upgrading photoelectrochemical materials and mitigation biotic-abiotic interface<sup>20</sup>, little attention has been given to strategic regulation of electron distribution to improve the performance of microbial cell factories. To address these bottlenecks, a programmable photosynthesis system was developed, capable of converting one-carbon substrates into a series of chemicals by rationally controlling electron distribution through an energy adapter. This system features user-defined functions and plug-and-play capabilities, serving as a foundational platform with multiple composability and extendibility, thereby facilitating the production of various biofuels and biochemicals. Future refinements in this programmable photosynthesis system will focus on the development of energy molecules-specific biosensors and energy levels-optimized oscillators. These advancements will enable the fine-tuning of the photosynthetic platform to meet the needs of a wide range of synthetic biology applications.

The essence of nature has been effectively utilized in different new-to-nature research fields, leading to numerous remarkable achievements<sup>13</sup>. In this study, the new-to-nature photosynthesis system was developed. Future efforts to enhance the new-to-nature photosynthesis system should focus on the following aspects: (i) improving the light-harvesting efficiency of the photosystem; (ii) enhancing carbon flux within the dark reaction; (iii) optimizing the intelligent coordination of the energy adapter; (iv) minimizing crosstalk with native energy metabolism; (v) developing fine-tuning toolkits for metabolic energy levels. By addressing these aspects, the new-to-nature photosynthesis system provides a roadmap for transforming non-photosynthetic microbes into novel photosynthetic life forms, offering a green and sustainable solution for enhancing the utilization of one-carbon substrates in the future.

## Methods

### Strains and plasmids

All strains, plasmids, and the information of genes and promoters used in this study were listed in Supplementary Datas 1–3. *E. coli* JM109 was used as the host to construct the plasmids. *E. coli* BL21(DE3) and plasmid pET28a were used for overexpressing and purifying ClFDH, niCAR, mmCAR, stAckA, mtAckA, mtASD, ecASD, nmGapN, ecGap2, ecProA, FLS\*, scDHAK, ecMgsA, bsMgsA, tsMgsA, pvMgsA, caADH1, mjLDH, eclDH, ssDDH, and FR. *E. coli* W3110 was used as the host for acetone, malate, and  $\alpha$ -ketoglutarate production. The plasmid pEtac was used to overexpress anchor proteins, backbone proteins, and heterologous proteins (ChlH, ChlI, ChlD, and Gun4). The plasmid pEM was used to overexpress a series of candidate target proteins (the limiting target proteins for ATP and NADH generation). The plasmid PJO1 was used to test the effectiveness of a series of candidate promoters for sensing the decrease of intracellular ATP and NADH levels and protein phase separation element A-IDP. The plasmid pCDR was used for combinatorial expression of thIA, YbgC, and Adc, or combinatorial expression of afPYC and asMDH, or combinatorial expression of afPYC, ecCS, ecACN, and eclDH. Ampicillin (100  $\mu$ g/mL), kanamycin (50  $\mu$ g/mL), or spectinomycin (50  $\mu$ g/mL) were added according to the introduced plasmids.

### Culture conditions

Luria-Bertani (LB) medium and plates were used for culturing strains. Terrific broth (TB) medium was used for culturing strains with pathway enzyme expression. 0.5 mM isopropyl- $\beta$ -D-thiogalactoside (IPTG) was added to induce the expression of enzymes when the cells grew to an OD<sub>600</sub> of 0.6–0.8. For testing the effectiveness of the light reaction, an LB medium containing 10 mM CH<sub>3</sub>OH and an appropriate antibiotic was used for culturing strain TL-NPM\*. The initial OD<sub>600nm</sub> value was 0.05. After 3 h cultivation at 37 °C, 0.25 mM IPTG, 1 mM  $\delta$ -aminolevulinic acid (ALA), and 1 mM Mg<sup>2+</sup> (equimolar mixture of MgCl<sub>2</sub> and MgSO<sub>4</sub>) were added and then transfer to shake flasks under dark and blue light illumination at 30 °C for detecting the growth performance and intracellular metabolic energy levels. NBS minimal medium (3.5 g/L KH<sub>2</sub>PO<sub>4</sub>, 5.0 g/L K<sub>2</sub>HPO<sub>4</sub>, 3.5 g/L (NH<sub>4</sub>)<sub>2</sub>HPO<sub>4</sub>, 0.25 g/L MgSO<sub>4</sub>·7H<sub>2</sub>O, 15 mg/L CaCl<sub>2</sub>·2H<sub>2</sub>O, 0.5 mg/L vitamin B1, 1 ml/L trace element solution (1.6 g/L FeCl<sub>3</sub>, 0.2 g/L CoCl<sub>2</sub>·6H<sub>2</sub>O, 0.1 g/L CuCl<sub>2</sub>, 0.2 g/L ZnCl<sub>2</sub>·4H<sub>2</sub>O, 0.2 g/L NaMnO<sub>4</sub>, 0.05 g/L H<sub>3</sub>BO<sub>3</sub>, dissolve in 0.1 M HCl) containing 50 mM NaHCO<sub>3</sub> (NaH<sup>13</sup>CO<sub>3</sub> was used for <sup>13</sup>C-labeling analysis), 5% glucose, 1 mM thiamine pyrophosphate (TPP), and appropriate antibiotic was used to test the effectiveness of ADRP in vivo. NBS minimal medium containing 50 mM NaHCO<sub>3</sub> (NaH<sup>13</sup>CO<sub>3</sub> was used for <sup>13</sup>C-labeling analysis), 10 mM CH<sub>3</sub>OH, 1 mM TPP, 1 mM ALA and Mg<sup>2+</sup> (equimolar mixture of MgCl<sub>2</sub> and MgSO<sub>4</sub>), and appropriate antibiotic was used to test the effectiveness of photosynthesis system in *E. coli* cell. NBS minimal medium containing NaHCO<sub>3</sub> and CH<sub>3</sub>OH (see below), 1 mM TPP, 1 mM ALA, and Mg<sup>2+</sup>, and an appropriate antibiotic was used for acetone, malate, and  $\alpha$ -ketoglutarate production.

For determining acetone, malate, and  $\alpha$ -ketoglutarate production, *E. coli* strains were grown aerobically in TB medium, and 0.5 mM IPTG was added at the mid-log phase. After 24 h, these cells were collected (washing 3 times with PBS buffer to remove residual medium components on the cell surface) and transferred to a 200 mL serum bottle with a 100 mL working volume. The microaerobic condition was achieved by purging the headspace with mixed gas (10% O<sub>2</sub> and 90% N<sub>2</sub>). The initial pH of the NBS minimal medium was controlled at 7.0. The initial OD<sub>600nm</sub> value was 18 (1 OD<sub>600nm</sub> = 0.33 g/L dry cells weight, DCW<sup>49</sup>). The representative metabolic engineering strategies for the production of acetone, malate, and  $\alpha$ -ketoglutarate were summarized in Supplementary Data 4. For a 5 L bioreactor scale, cells were initially grown in TB medium (rotate rate 400 rpm, airflow 0.5 volume of air per volume of liquid per min, off-gas analyzers (Shanghai Baiyuan Bio) were used to measure total CO<sub>2</sub> emissions) for 16 h and then collected (washing 3 times with PBS buffer to remove residual medium components on the cell surface). These cells were transferred to a 5 L bioreactor with a 2.5 L working volume (rotate rate 400 rpm, 96 h). The initial pH of the NBS minimal medium was controlled at 7.0 (NH<sub>3</sub>-H<sub>2</sub>O was used to control the pH to 7.0), and the initial OD<sub>600nm</sub> value was 18. The final concentrations of 100 mM NaHCO<sub>3</sub> and 200 mM CH<sub>3</sub>OH (NaH<sup>13</sup>CO<sub>3</sub> and <sup>13</sup>CH<sub>3</sub>OH were used for <sup>13</sup>C-labeling analysis) were added initially and supplemented every 12 h. Blue light ( $\lambda$  is 450 - 460 nm) illumination intensity was controlled at 25 mW/cm<sup>2</sup>.

### Genetic manipulations

CRISPR-Cas9 based technology was applied to edit the genome, such as deleting or replacing genetic sequences genes to construct *E. coli* mutants<sup>57</sup>. All plasmids were constructed using Gibson assembly and basic molecular cloning techniques<sup>50</sup>. The genes encoding crePsbA, PufL, soePsbA, ChlH, ChlI, ChlD, Gun4, niCAR, mmCAR, stAckA, mtAckA, mtASD, nmGapN, bsMgsA, tsMgsA, pvMgsA, caADH1, mjLDH, ssDDH, ThIA, Adc, and YbgC were artificially synthesized by Talen-bio Scientific Co., Ltd (with codon optimization for *E. coli*). The genes encoding NuoA, NuoK, NuoJ, NuoE, AppB, AtpF, AtpH, CydB, FdnI, UbiK, UbiV, YceJ, YodB, NadB, NadD, PncA, PncC, UmpH, ecASD, ecGap2, ecProA, ecMgsA, ecLDH, CS, CAN, and IDH were amplified by PCR from genomic DNA of *E. coli* MG1655. A series of PJ01 plasmids were constructed by replacing the promoter region to test the effectiveness of candidate promoters. A series of F7K plasmids were constructed by replacing the RBS region to obtain a series of discharging regulation plasmids. To construct the acetone biosynthesis pathway, the genes encoding ThIA, YbgC, and Adc<sup>51</sup> were amplified and assembled to obtain plasmid pCDR-TYA. Similarly, the genes encoding AfPYC and AsMDH were amplified and assembled to obtain plasmid pCDR-PM for constructing malate biosynthesis pathway, and the genes encoding AfPYC, EcCS, EcACN, and EcLDH<sup>52</sup> were amplified and assembled to obtain plasmid pCDR-PCAI for constructing  $\alpha$ -ketoglutarate biosynthesis pathway. Key primers used in this study for genetic manipulations were listed in Supplementary Data 5.

### Construction of ADRP in vitro

First, formyl phosphate was assayed colorimetrically by the hydroxamate method<sup>53</sup>. One unit of AckA activity was defined as the increase of one unit of A<sub>505nm</sub> per minute. NADH or NADPH concentrations were monitored as in the stAckA-ecASD cascade assay. One unit of ecASD activity was defined as the decrease of 1  $\mu$ mol NADH or NADPH per minute by measuring A<sub>340nm</sub>. Methylglyoxal was assayed by colorimetry<sup>54</sup>. One unit of MgsA activity was defined as the increase of one unit of A<sub>555nm</sub> per minute. NADH concentrations were monitored as in the LDH activity assay. One unit of LDH activity was defined as the increase of 1  $\mu$ mol NADH per minute by measuring A<sub>340nm</sub>. All enzyme activities were determined on a SpectraMax M3 microplate reader (Molecular Devices, Sunnyvale, CA). The specific activities of candidate

pathway enzymes in the C1 and C3 modules were presented in Supplementary Datas 6, 7. Then, six pathway enzymes were purified using His GraviTrap Kit<sup>55</sup>. The purified proteins, including ClFDH, FR, FLS\*, ScDHAK, BsMgsA, and EcLDH were combined with an assay mix of 50 mM Tris-HCl buffer (pH = 7.5), 5 mM MgCl<sub>2</sub>, 2 mM ATP, 2 mM NADH, 1 mM TPP, and 100 mM NaHCO<sub>3</sub>. The one-pot catalytic reaction was terminated after 18 h at 30 °C. Pyruvate was determined by HPLC and LC-MS.

### Assay of intracellular metabolic energy

To prepare samples for ATP and NADH assay, *E. coli* cells at each sampling time point were collected and washed (4000  $\times$  g, 5 min, 4 °C) using phosphate-buffered saline. ATP Assay Kit S0027 (Beyotime Biotechnology) was used to determine the intracellular ATP concentration. The intracellular ATP concentration was calculated according to the ATP standard curve. NADH Assay Kit with WST-8 (Beyotime Biotechnology) was used to determine the intracellular NADH concentration. The intracellular NADH concentration was calculated according to the NADH standard curve. In addition, ATP fluorescent sensor QUEEN2m<sup>56</sup> and NADH fluorescent sensor Frex<sup>57</sup> were used to detect the intracellular ATP and NADH, respectively.

### Assay of RhB and congo red degradation

The Mg (II) protoporphyrin IX dipotassium salt was purchased from Frontier Specialty Chemicals and was used as the MgP standard for photocatalytic degradation of RhB and Congo red. MgP, RhB, and congo red were dissolved in methanol (as an electron sacrificial agent for MgP), respectively. 15 mg/L MgP was mixed with 50 mg/L RhB and 50 mg/L congo red to obtain a 2 mL photocatalytic degradation mixture, respectively. After 90 min of illumination with blue light, samples were collected to detect RhB and congo red degradation in 553 and 540 nm using a SpectraMax M3 plate reader, respectively.

### Assay of membrane potential and proton gradient

For the preparation of membrane fractions, engineered *E. coli* cells in the stationary phase were collected and disrupted by sonication. The insoluble fractions were removed by centrifugation at 12,000  $\times$  g, 4 °C for 10 min, and the supernatant was applied to ultracentrifugation<sup>58</sup> (Beckman Colter Optima™ XPN) at 250,000  $\times$  g, 4 °C for 1 h. The membrane fraction was resuspended in the extraction buffer (pH 7.5) containing 20 mM Tris-HCl, 150 mM NaCl, 10 mM imidazole, 10% glycerol, and 1.0% (wt/vol) *n*-dodecyl- $\beta$ -D-maltopyranoside (DDM) for 2 h at 4 °C to prepare membrane protein samples. The obtained membrane fraction was resuspended in buffer (10 mM Tris-HCl, 1 mM EDTA, 1 mM DTT, 15% glycerol, pH = 7.0) for further use. For membrane potential assay, the reaction mixture contained 50 mM MOPS (pH = 7.3), 10 mM MgCl<sub>2</sub>, 50 mM KCl, 2 mM methanol, 2  $\mu$ M oxonol VI, membrane sample (400  $\mu$ g protein/mL). After the signal had stabilized, the reaction was started by adding 0.2 mM NADH or blue light illumination for 10 min. For the proton gradient assay, the reaction mixture contained 50 mM MOPS (pH = 7.3), 10 mM MgCl<sub>2</sub>, 50 mM KCl, 2 mM methanol, 2  $\mu$ M ACMA, and the membrane sample (150  $\mu$ g protein/mL). Similarly, 0.2 mM NADH or blue light illumination for 10 min was used to start the reaction. When appropriate, the uncoupler FCCP was added to a final concentration of 2  $\mu$ M and 10  $\mu$ M to release the membrane potential and proton gradient, respectively. The antimycin A3 was added to a final concentration of 2  $\mu$ M to inhibit complex III in the electron transport chain. The oxonol VI and ACMA signals were detected using SpectraMax M3 microplate reader<sup>59,60</sup>.

### Flow cytometry assays

The engineered *E. coli* cells were gathered by centrifugation (4 °C, 5 min, 4000  $\times$  g), and then washed and resuspended in cold PBS. Samples were incubated with 10  $\mu$ L of dyes DiBAC<sub>4</sub>(3) and DiSC<sub>3</sub>(5) avoiding light for 10 min, and then washed twice with PBS and

resuspended to an OD<sub>600</sub> of 0.3. BD FACSArica™ III cytometer (BD Biosciences, USA) was used to determine the fluorescence of each sample. DiBAC<sub>4</sub>(3) and DiSC<sub>3</sub>(5) were detected in the FITC channel (488 nm EL, 530/30 nm EF) and APC channel (638 nm EL, 660/20 nm EF), respectively. In addition, the EGFP fluorescence of cells was detected in the FITC channel after being gathered, washed, and resuspended. The PI (propidium iodide) signals of *E. coli* cells were detected in the PerCP-Cy5-5-A channel after incubation with PI dye for 15 min. The Alexa Fluor 647 (Beyotime Biotechnology) fluorescence of *E. coli* spheroplast was detected in the APC channel after incubation for 1 h. All data were analyzed by FlowJo software (FlowJo-V10).

### Fluorescence intensity and microscope image characterization

For fluorescence intensity assay, engineered *E. coli* cells were incubated in 24 deep-well plates containing 3 mL of LB medium with appropriate IPTG and antibiotics at 37 °C, 700 rpm in a Titramax 1000 incubator (Heidolph Instruments). Samples were taken at the sampling time point and diluted 1:4 in 200 µL fresh LB medium and then measured using a SpectraMax M3 microplate reader (Molecular Devices). The excitation and emission wavelengths of EGFP were set at 480 ± 10 nm and 515 ± 10 nm, respectively. The mKate intensity was measured at an excitation wavelength 588 ± 10 nm and an emission wavelength 645 ± 10 nm. All fluorescence was normalized with cell density by measuring the absorbance at 600 nm. For the fluorescence microscope, engineered *E. coli* cells were collected by centrifugation (4000 × g, 5 min) and resuspended in PBS, of which 2 µL was sampled onto a glass slide and covered by 2% LB agar to fix the cells. A Fluorescence microscope was performed with a laser confocal microscope (Leica TCS SP8) using a × 60 oil objective lens. The width and length of *E. coli* cells were measured by manual tracing in LAS AF Lite software. Pixel intensity data of EGFP, mKate, and FM4-64 were collected via LAS AF Lite software. The cells were imaged by Leica TCS SP8, and the quantification of CAPI and DAPI were performed in Image J (NIH, <http://rsbweb.nih.gov/ij/>) using fluorescence images of cells. Microsoft Excel 2016 and Origin 2019 were used for statistical analyses.

### Analytical methods

The intracellular MgP formation was measured by plant magnesium protoporphyrin IX (Mg-ProtoIX) ELISA Kit (Shanghai Kang Lang Biotech Co., Ltd). The OD<sub>600nm</sub> was measured by spectrophotometer, and DCW was calculated according to a calibration line from the optical density (600 nm) (1 OD<sub>600nm</sub> = 0.33 g/L DCW<sup>49</sup>). For photoelectrochemical measurements, the photocurrent of *E. coli* cells lyophilized powder was monitored by an electrochemical workstation (CHI 760E, CH Instruments, USA) under xenon lamp illumination (λ > 400 nm, turn on 20 s and turn off 20 s for four cycles)<sup>26</sup>. The surface photovoltage (SPV) and surface photocurrent (SPC) of MgP powder and *E. coli* cells lyophilized powder were measured by surface photovoltage spectrometer (CEL-SPS1000, CEALight Instruments, China). For transient absorption measurements, the transient absorption spectra of MgP and *E. coli* cells was based on the pump-probe transient absorption spectrometer (Helios, Ultrafast System)<sup>61</sup>. The pump pulse was tuned to a wavelength of 415 nm to excite MgP and study the reaction dynamics. The solution of MgP and the suspension of *E. coli* cells were used as samples for transient absorption measurements. To determine the concentration of metabolites, the HPLC system (Dionex UltiMate 3000 Series, Thermo Scientific, USA) was used to determine the concentration of pyruvate and malate. This system was equipped with an Aminex HPX-87H ion-exchange column (7.8 × 300 mm, Bio-Rad Laboratories, USA) at 35 °C with 5 mM sulfuric acid as mobile phase. The injection volume was 10 µL, and the flow rate was 0.6 mL/min. The concentration of acetone was analyzed by gas chromatograph<sup>51</sup>. The intracellular pyruvate, acetoacetate, oxaloacetate, α-ketoglutarate, and citrate contents were determined by HPLC<sup>62,63</sup>. To prepare samples for LC-MS detection, cell suspensions

were collected, quenched, and washed with 160 µL cold (−10 °C) aqueous methanol solution (60%, v/v). By adding 200 µL 0.3 M KOH and cell lysis buffer, the mixture was frozen using liquid nitrogen for 5 min and stored at −80 °C refrigerator. Samples were thawed on ice and neutralized by adding 4 µL acetic acid. After centrifugation (12,000 × g, −10 °C) for 10 min, the supernatant was transferred to a clean centrifuge tube for LC-MS detection. Total carbon labeling was calculated according to the formula:

$$\text{labelled fraction} = \frac{\sum_i^n mi^*i}{\sum_i^n mi^*n} \quad (5)$$

where \* indicates multiply<sup>29</sup>. The methods for transcriptomic sequencing analysis were presented in Supplementary Note 18.

### Adaptive laboratory evolution

Long-term adaptive laboratory evolution was carried out in an automatic microbial adaptive evolution instrument (EVOL cell). The engineered strain *E. coli* TC-F2 was spotted on NBS-CMFG plate, and three colonies were selected and cultivated in NBS-CMFG liquid medium (NBS medium with 100 mM NaHCO<sub>3</sub> (equivalent to CO<sub>2</sub>), 200 mM methanol, 200 mM formate, and 50 mM glucose) at 37 °C and 25 mW/cm<sup>2</sup> blue light illumination for 12 h. Three generations were conducted under the same conditions. The engineered strain *E. coli* TC-F2 cells were then transferred to a fresh NBS-CMFG liquid medium with an initial OD<sub>600</sub> of ~0.05. After cultivation of 12 h, *E. coli* TC-F2 cells were transferred into a fresh NBS-CMFG liquid medium with gradually decreased glucose concentrations (50, 25, 12.5, 10, 7.5, 5, 2.5 and 1.25 mM, respectively). Then, *E. coli* cells were transferred to NBS-CMFG liquid medium without glucose for further culture. This initial light-driven one-carbon trophic *E. coli* TC-F3 was obtained, which grew on one-carbon substrates NaHCO<sub>3</sub> (equivalent to CO<sub>2</sub>), methanol, and formate as carbon sources with a maximum OD<sub>600</sub> of 0.417. The growth performance of evolved strain *E. coli* TC-F3 was tested and the doubling time of evolved strains was calculated according to the equation in Supplementary Fig. 52.

### Statistical and reproducibility

All data in this study were expressed as mean ± s.d. The data analysis and graphing were performed by Origin 2019. The significance of the two groups were determined by a two-tailed Student's *t* test and paired sample analysis through SPSS statistics software. Each experiment in this study was repeated at least three times of biological independent experiments.

### Reporting summary

Further information on research design is available in the Nature Portfolio Reporting Summary linked to this article.

### Data availability

The raw data of the RNAseq are available at NCBI under accession PRJNA1054475. Source data are provided with this paper, which is also available at Figshare [<https://doi.org/10.6084/m9.figshare.27931263>]. Source data are provided in this paper.

### References

1. Lv, J. et al. Solar utilization beyond photosynthesis. *Nat. Rev. Chem.* **7**, 91–105 (2022).
2. De Souza, A. P. et al. Soybean photosynthesis and crop yield are improved by accelerating recovery from photoprotection. *Science* **377**, 851–854 (2022).
3. Mirkovic, T. et al. Light absorption and energy transfer in the antenna complexes of photosynthetic organisms. *Chem. Rev.* **117**, 249–293 (2017).
4. Zhou, Y. J., Kerkhoven, E. J. & Nielsen, J. Barriers and opportunities in bio-based production of hydrocarbons. *Nat. Energy* **3**, 925–935 (2018).

5. Kim, S. et al. Growth of *E. coli* on formate and methanol via the reductive glycine pathway. *Nat. Chem. Biol.* **16**, 538–545 (2020).
6. Blankenship, R. E. et al. Comparing photosynthetic and photovoltaic efficiencies and recognizing the potential for improvement. *Science* **332**, 805–809 (2011).
7. Li, C., Yin, L., Wang, J., Zheng, H. & Ni, J. Light-driven biosynthesis of volatile, unstable and photosensitive chemicals from CO<sub>2</sub>. *Nat. Synth.* **2**, 960–971 (2023).
8. Tan, C., Tao, F. & Xu, P. Direct carbon capture for the production of high-performance biodegradable plastics by cyanobacterial cell factories. *Green Chem.* **24**, 4470–4483 (2022).
9. Kanno, M., Carroll, A. L. & Atsumi, S. Global metabolic rewiring for improved CO<sub>2</sub> fixation and chemical production in cyanobacteria. *Nat. Commun.* **8**, 1–11 (2017).
10. Tan, C., Xu, P. & Tao, F. Carbon-negative synthetic biology: challenges and emerging trends of cyanobacterial technology. *Trends Biotechnol.* **40**, 1488–1502 (2022).
11. Zheng, T. et al. Upcycling CO<sub>2</sub> into energy-rich long-chain compounds via electrochemical and metabolic engineering. *Nat. Catal.* **5**, 388–396 (2022).
12. Chen, H., Dong, F. & Minter, S. D. The progress and outlook of bioelectrocatalysis for the production of chemicals, fuels and materials. *Nat. Catal.* **3**, 225–244 (2020).
13. Proppe, A. H. et al. Bioinspiration in light harvesting and catalysis. *Nat. Rev. Mater.* **5**, 828–846 (2020).
14. Cestellos-Blanco, S., Zhang, H., Kim, J. M., Shen, Y.-X. & Yang, P. Photosynthetic semiconductor biohybrids for solar-driven biocatalysis. *Nat. Catal.* **3**, 245–255 (2020).
15. Deng, J. et al. Nanowire photoelectrochemistry. *Chem. Rev.* **119**, 9221–9259 (2019).
16. Liu, C., Colon, B. C., Ziesack, M., Silver, P. A. & Nocera, D. G. Water splitting-biosynthetic system with CO<sub>2</sub> reduction efficiencies exceeding photosynthesis. *Science* **352**, 1210–1213 (2016).
17. Chowdhury, F. A., Trudeau, M. L., Guo, H. & Mi, Z. A photochemical diode artificial photosynthesis system for unassisted high efficiency overall pure water splitting. *Nat. Commun.* **9**, 1–9 (2018).
18. Guo, J. et al. Light-driven fine chemical production in yeast biohybrids. *Science* **362**, 813–816 (2018).
19. Sakimoto, K. K., Wong, A. B. & Yang, P. Self-photosensitization of nonphotosynthetic bacteria for solar-to-chemical production. *Science* **351**, 74–77 (2016).
20. Kornienko, N., Zhang, J. Z., Sakimoto, K. K., Yang, P. & Reisner, E. Interfacing nature’s catalytic machinery with synthetic materials for semi-artificial photosynthesis. *Nat. Nanotechnol.* **13**, 890–899 (2018).
21. Guan, X. et al. Maximizing light-driven CO<sub>2</sub> and N<sub>2</sub> fixation efficiency in quantum dot-bacteria hybrids. *Nat. Catal.* **5**, 1019–1029 (2022).
22. Liu, C. et al. Nanowire-bacteria hybrids for unassisted solar carbon dioxide fixation to value-added chemicals. *Nano Lett.* **15**, 3634–3639 (2015).
23. Wang, Q., Kalathil, S., Pornrungraj, C., Sahm, C. D. & Reisner, E. Bacteria-photocatalyst sheet for sustainable carbon dioxide utilization. *Nat. Catal.* **5**, 633–641 (2022).
24. Torella, J. P. et al. Efficient solar-to-fuels production from a hybrid microbial-water-splitting catalyst system. *Proc. Natl. Acad. Sci. USA* **112**, 2337–2342 (2015).
25. Yu, W. et al. Solar-driven producing of value-added chemicals with organic semiconductor-bacteria biohybrid system. *Research* **2022**, 9834093 (2022).
26. Wang, B., Jiang, Z., Yu, J. C., Wang, J. & Wong, P. K. Enhanced CO<sub>2</sub> reduction and valuable C<sub>2+</sub> chemical production by a CdS-photosynthetic hybrid system. *Nanoscale* **11**, 9296–9301 (2019).
27. Zhang, J., Liu, L. & Chen, X. Pushing hybrids to the limits. *Nat. Catal.* **5**, 975–976 (2022).
28. Xiao, K. et al. Panoramic insights into semi-artificial photosynthesis: origin, development, and future perspective. *Energy Environ. Sci.* **15**, 529–549 (2022).
29. Hu, G. et al. Light-driven CO<sub>2</sub> sequestration in *Escherichia coli* to achieve theoretical yield of chemicals. *Nat. Catal.* **4**, 395–406 (2021).
30. Peterson, A., Baskett, C., Ratcliff, W. C. & Burnetti, A. Using light for energy: examining the evolution of phototrophic metabolism through synthetic construction. Preprint at <https://doi.org/10.1101/2022.12.06.519405> (2023).
31. Pennisi, E. Yeast are engineered to thrive on light. *Science* **380**, 231 (2023).
32. Chen, P. et al. A plant-derived natural photosynthetic system for improving cell anabolism. *Nature* **612**, 546–554 (2022).
33. Cournoyer, J. E. et al. Engineering artificial photosynthetic life-forms through endosymbiosis. *Nat. Commun.* **13**, 1–14 (2022).
34. Kravchuk, V. et al. A universal coupling mechanism of respiratory complex I. *Nature* **609**, 808–814 (2022).
35. Chen, G. E. et al. Complete enzyme set for chlorophyll biosynthesis in *Escherichia coli*. *Sci. Adv.* **4**, 1–8 (2018).
36. Ding, Q. et al. Light-powered *Escherichia coli* cell division for chemical production. *Nat. Commun.* **11**, 1–14 (2020).
37. Gao, C. et al. Programmable biomolecular switches for rewiring flux in *Escherichia coli*. *Nat. Commun.* **10**, 1–12 (2019).
38. Zhou, P. et al. Engineered artificial membraneless organelles in *Saccharomyces cerevisiae* to enhance chemical production. *Angew. Chem. Int. Ed.* **62**, e202215778 (2023).
39. Kirst, H., Formighieri, C. & Melis, A. Maximizing photosynthetic efficiency and culture productivity in cyanobacteria upon minimizing the phycobilisome light-harvesting antenna size. *BBA Bioenerg.* **1837**, 1653–1664 (2014).
40. Qin, X. et al. Structure of a green algal photosystem I in complex with a large number of light-harvesting complex I subunits. *Nat. Plants* **5**, 263–272 (2019).
41. Walter, J. M., Greenfield, D., Bustamante, C. & Liphardt, J. Light-powering *Escherichia coli* with proteorhodopsin. *Proc. Natl. Acad. Sci. USA* **104**, 2408–2412 (2007).
42. Claassens, N. J., Volpers, M., dos Santos, V. A., van der Oost, J. & de Vos, W. M. Potential of proton-pumping rhodopsins: engineering photosystems into microorganisms. *Trends Biotechnol.* **31**, 633–642 (2013).
43. Singh, A. K. & Mallick, N. Advances in cyanobacterial polyhydroxyalkanoates production. *FEMS Microbiol. Lett.* **364**, fnx189 (2017).
44. Nielsen, J. & Keasling, J. D. Engineering cellular metabolism. *Cell* **164**, 1185–1197 (2016).
45. Kuk, S. K. et al. Photoelectrochemical reduction of carbon dioxide to methanol through a highly efficient enzyme cascade. *Angew. Chem. Int. Ed.* **56**, 3827–3832 (2017).
46. Zhang, H. et al. Bacteria photosensitized by intracellular gold nanoclusters for solar fuel production. *Nat. Nanotechnol.* **13**, 900–905 (2018).
47. Miller, T. E. et al. Light-powered CO<sub>2</sub> fixation in a chloroplast mimic with natural and synthetic parts. *Science* **368**, 649–654 (2020).
48. Chen, F. Y., Jung, H. W., Tsuei, C. Y. & Liao, J. C. Converting *Escherichia coli* to a synthetic methylotroph growing solely on methanol. *Cell* **182**, 933–946 (2020).
49. Dong, X. et al. Metabolic engineering of *Escherichia coli* W3110 to produce L-malate. *Biotechnol. Bioeng.* **114**, 656–664 (2017).
50. Guo, L. et al. Engineering *Escherichia coli* lifespan for enhancing chemical production. *Nat. Catal.* **3**, 307–318 (2020).
51. May, A. et al. A modified pathway for the production of acetone in *Escherichia coli*. *Metab Eng.* **15**, 218–225 (2013).

52. Chen, X., Dong, X., Liu, J., Luo, Q. & Liu, L. Pathway engineering of *Escherichia coli* for  $\alpha$ -ketoglutaric acid production. *Biotechnol. Bioeng.* **117**, 2791–2801 (2020).
53. Mejillano, M. R., Jahansouz, H., Matsunaga, T. O., Kenyon, G. L. & Himes, R. H. Formation and utilization of formyl phosphate by N10-formyltetrahydrofolate synthetase: evidence for formyl phosphate as an intermediate in the reaction. *Biochemistry* **28**, 5136–5145 (1989).
54. Hopper, D. J. & Cooper, R. A. J. B. J. The purification and properties of *Escherichia coli* methylglyoxal synthase. *Biochem. J.* **128**, 321–329 (1972).
55. Tong, T. et al. A biosynthesis pathway for 3-hydroxypropionic acid production in genetically engineered *Saccharomyces cerevisiae*. *Green Chem.* **23**, 4502–4509 (2021).
56. Yaginuma, H. et al. Diversity in ATP concentrations in a single bacterial cell population revealed by quantitative single-cell imaging. *Sci. Rep.* **4**, 6522 (2014).
57. Zhao, Y. et al. Genetically encoded fluorescent sensors for intracellular NADH detection. *Cell Metab.* **14**, 555–566 (2011).
58. Gao, S. et al. Employing NaChBac for cryo-EM analysis of toxin action on voltage-gated Na<sup>+</sup> channels in nanodisc. *Proc. Natl. Acad. Sci. USA* **117**, 14187–14193 (2020).
59. Kao, M.-C., Nakamaru-Ogiso, E., Matsuno-Yagi, A. & Yagi, T. Characterization of the membrane domain subunit NuoK (ND4L) of the NADH-quinone oxidoreductase from *Escherichia coli*. *Biochemistry* **44**, 9545–9554 (2005).
60. Kao, M.-C. et al. Characterization of the membrane domain subunit NuoJ (ND6) of the NADH-quinone oxidoreductase from *Escherichia coli* by chromosomal DNA manipulation. *Biochemistry* **44**, 3562–3571 (2005).
61. Hu, Q. et al. Ultrafast electron transfer in Au-cyanobacteria hybrid for solar to chemical production. *ACS Energy Lett.* **8**, 677–684 (2023).
62. Chen, X., Ma, D., Liu, J., Luo, Q. & Liu, L. Engineering the transmission efficiency of the noncyclic glyoxylate pathway for fumarate production in *Escherichia coli*. *Biotechnol. Biofuels* **13**, 132 (2020).
63. Yamato, S. et al. High-performance liquid chromatography determination of ketone bodies in human plasma by precolumn derivatization with *p*-nitrobenzene diazonium fluoroborate. *Anal. Biochem.* **384**, 145–150 (2009).
- Province 2021RC4063 (to G.L.), and Basic Research Center for Synthetic Biology of Jiangsu Province BK20233003 (to L.L.).

### Author contributions

T.T., X.C., G.L. and L.L. conceived the project and wrote the paper. T.T., X.C., K.T. and W.M. designed and performed all the experiments. T.T., X.C., C.G., W.S., J.W. and X.W. analyzed the results.

### Competing interests

The authors declare no competing interests.

### Additional information

**Supplementary information** The online version contains supplementary material available at <https://doi.org/10.1038/s41467-024-55498-y>.

**Correspondence** and requests for materials should be addressed to Gao-Qiang Liu or Liming Liu.

**Peer review information** *Nature Communications* thanks Jun Ni and the other anonymous reviewer(s) for their contribution to the peer review of this work. A peer review file is available.

**Reprints and permissions information** is available at <http://www.nature.com/reprints>

**Publisher's note** Springer Nature remains neutral with regard to jurisdictional claims in published maps and institutional affiliations.

**Open Access** This article is licensed under a Creative Commons Attribution-NonCommercial-NoDerivatives 4.0 International License, which permits any non-commercial use, sharing, distribution and reproduction in any medium or format, as long as you give appropriate credit to the original author(s) and the source, provide a link to the Creative Commons licence, and indicate if you modified the licensed material. You do not have permission under this licence to share adapted material derived from this article or parts of it. The images or other third party material in this article are included in the article's Creative Commons licence, unless indicated otherwise in a credit line to the material. If material is not included in the article's Creative Commons licence and your intended use is not permitted by statutory regulation or exceeds the permitted use, you will need to obtain permission directly from the copyright holder. To view a copy of this licence, visit <http://creativecommons.org/licenses/by-nc-nd/4.0/>.

© The Author(s) 2024

### Acknowledgements

This work is supported by the National Natural Science Foundation of China 22038005 (to L.L.), the Major Project of Natural Science Foundation of Jiangsu Province BK20220022 (to L.L.), the Frontier Leading Technology Basic Research Special of Jiangsu Province BK20212013 (to L.L.), the Project of Science and Technology Innovation Team of Hunan